
A Composite Activation Function for Learning Stable Binary Representations

Seokhun Park¹, Choemun Kim¹, Kwanho Lee¹, Sehyun Park¹, Insung Kong², Yongdai Kim¹

¹Department of Statistics, Seoul National University

²Department of Applied Mathematics, University of Twente

{shrdid, kimchoemun, khlee0527}@snu.ac.kr, insung.kong@utwente.nl,
ps_hyen@snu.ac.kr, ydkim0903@gmail.com

Abstract

Activation functions play a central role in neural networks by shaping internal representations. Recently, learning binary activation representations has attracted significant attention due to their advantages in computational and memory efficiency, as well as interpretability. However, training neural networks with Heaviside activations remains challenging, as their non-differentiability obstructs standard gradient-based optimization. In this paper, we propose *Heavy-Tailed Activation Function (HTAF)*, a smooth approximation to the Heaviside function that enables stable training with gradient-based optimization. We construct HTAF as a sigmoid-hyperbolic tangent composite function and theoretically show that it maintains a large gradient mass around zero inputs while exhibiting slower gradient decay in the tail regions. We show that Spiking Neural Networks, Binary Neural Networks and Deep Heaviside neural Networks can be trained stably using HTAF with gradient-based optimization. Finally, we introduce Implicit Concept Bottleneck Models (ICBMs), an interpretable image model that leverages HTAF to induce discrete feature representations. Extensive experiments across various architectures and image datasets demonstrate that ICBM enables stable discretization while achieving prediction performance comparable to or better than standard models.

1 Introduction

Activation functions play a central role in neural networks by transforming continuous signals into structured representations that enable effective learning and prediction. Through this transformation, activation functions critically influence not only prediction performance ([4, 21]), but also the robustness ([65, 74]) and interpretability of learned representations ([9, 17, 31, 18]). Early neural network models ([56]) were based on threshold-based activation functions, which are equivalent to the Heaviside activation function $x \mapsto \mathbb{I}(x \geq 0)$. However, such non-differentiable activations made gradient-based learning intractable. To address this issue, differentiable surrogate activation functions such as the sigmoid function were introduced ([58]). Subsequently, to mitigate the gradient vanishing problem, Rectified Linear Units (ReLU) became widely adopted ([20]).

Recently, the Heaviside activation function has attracted increasing attention again in the AI community due to their potential benefits in memory and computational efficiency ([77, 14, 52]), interpretability ([73, 79, 40]), and connections to biological neural networks ([83, 41, 66]). Furthermore, the Heaviside activation function is closely related to quantized and binarized neural networks ([11, 26, 52]), which have become increasingly important for energy-efficient deployment of large deep neural networks such as large language models (LLMs, [70, 44]).

Although the Heaviside activation function offers several advantages, training neural networks that use it with gradient-based optimization remains difficult because the function is inherently non-differentiable. To address this issue, a substantial body of work ([3, 41, 83, 28, 48]) has focused on developing methods for learning neural networks with the Heaviside activation function. [3] proposed Straight-Through Estimator (STE), which enables gradient-based optimization of non-differentiable functions by using surrogate gradients. While STE serves as a practical workaround, it introduces a mismatch between the forward and backward passes and often leads to biased or suboptimal optimization ([77]). Another approach is to replace the Heaviside activation function with a smooth surrogate ([28]), most notably the sigmoid function, and encourage the activations to approach binary values by increasing the slope or scale of the nonlinearity. While this approach enables the use of standard gradient-based optimization, it suffers from severe optimization instability ([19, 8]) including the gradient vanishing problem.

In this paper, we propose a novel smooth activation function, called *Heavy-Tailed Activation Function (HTAF)*, which closely approximates the Heaviside function while enabling stable and accurate training with standard gradient-based optimization. The key idea is to design an activation function that preserves a large gradient near zero (to approximate the Heaviside function closely), while allowing the gradient to decay slowly for large-magnitude inputs (to avoid the gradient vanishing problem). Specifically, HTAF has two parameters that allow the gradient magnitude in the tail regions to be adjusted without affecting the gradient near zero. That is, by adjusting these two parameters, HTAF allows the gradient in the tail region to decay more slowly, while still preserving a high gradient near zero.

As an application of HTAF, we consider two problems. Firstly, using HTAF, we propose a general learning framework for neural networks with the Heaviside activation function, including Spiking Neural Networks (SNNs, [66, 16, 45]), Binary Neural Networks (BNNs, [52, 55, 42]), and Deep Heaviside Neural Networks (DHNs, [34, 14]), enabling stable end-to-end optimization without surrogate gradients for activation functions. Second, we propose Implicit Concept Bottleneck Models (ICBMs), an extension of Concept Bottleneck Models (CBMs, [32]), which employ HTAF as the activation function in the final layer of the backbone feature extractor during training. HTAF encourages each feature to take values close to either zero or one. At inference time, HTAF is replaced by the Heaviside function, yielding exact binary activations and resulting in fully discrete and interpretable features without substantially sacrificing accuracy.

To sum up, our key contributions are summarized as follows.

1. We introduce *Heavy-Tailed Activation Function (HTAF)*, a novel smooth activation function, which approximates the Heaviside activation function.
2. We theoretically show that, by appropriately tuning its two parameters, HTAF can control the rate of gradient decay in tail regions while keeping a large gradient near zero, thereby enabling stable learning of deep neural networks (DNNs) with HTAF activation with standard gradient-based optimization.
3. We demonstrate that HTAF enables gradient-based learning of DNNs with the Heaviside activation function, allowing stable end-to-end optimization and improving prediction performance over existing training methods, including those based on surrogate gradients.
4. We propose Implicit Concept Bottleneck Models (ICBM), an interpretable image model that leverages HTAF to induce binary latent representations corresponding to implicit concepts. We show that the resulting model is interpretable while achieving competitive or improved prediction performance across various image datasets compared to non-interpretable models.

2 Related works

2.1 Deep Neural Networks with the Heaviside activation function

Heaviside-Activated Neural Networks and their advantages. DNNs with the Heaviside activation function have been widely studied in various neural network models, including Spiking Neural Networks (SNNs, [83, 16, 27]), Binary Neural Networks (BNNs, [52, 55]), and Deep Heaviside Neural Networks (DHNs, [34]). SNNs use the Heaviside function to model discrete spike generation, offering a biologically inspired and energy-efficient computation paradigm. Similarly, in BNNs,

activations and weights are constrained to binary values, allowing significant reductions in memory usage and computational cost. DHNs are standard deep neural networks employing the Heaviside activation function.

A key advantage of such models is their efficiency during inference. The output of the Heaviside activation function can be represented using a single bit, leading to substantial memory savings compared to floating-point representations. Moreover, multiplications can be simplified or eliminated, resulting in lightweight computations and faster inference.

Training methods. Methods for training neural networks with the Heaviside activation function can be broadly categorized into three approaches. The first approach ([3, 41, 83]) employs the Heaviside activation function together with surrogate gradients during training. A representative approach is Straight-Through Estimator (STE, [3]), which replaces the gradient of the Heaviside function with a smooth surrogate function during backpropagation while retaining the original hard thresholding in the forward pass. Although surrogate-gradient methods have been widely studied and adopted, learning neural networks with the Heaviside activation function via such approaches remains challenging. Specifically, the reliance on approximate rather than true gradients often leads to unstable optimization dynamics and degraded prediction performance ([77]).

The second line of work ([28, 7, 38]) approximates the Heaviside activation function with smooth activations to enable standard gradient-based optimization, most commonly using the sigmoid function. However, sigmoid-based approximations suffer from the well-known gradient vanishing problem ([19, 8]). Specifically, as the sigmoid becomes steeper around $x = 0$, inputs quickly enter saturation regimes where gradients vanish, resulting in unstable training or optimization stagnation.

Finally, another line of work ([12, 57, 25, 62, 6]) first trains conventional DNNs with a smooth activation function and then converts them post-hoc into SNNs or BNNs, thereby avoiding direct training with Heaviside activation function.

2.2 Concept Bottleneck Models

[32] introduced Concept Bottleneck Models (CBMs), a class of interpretable image models that incorporate human-interpretable concepts as intermediate representations. In CBMs, the model first predicts a set of predefined concepts and then uses them for class prediction, enabling transparency and intervention at the concept level.

However, CBMs often suffer from reduced prediction performance and limited practicality due to the requirement of concept annotations, which are costly to obtain. To address this, subsequent works have proposed label-free variants using pretrained models such as Contrastive Language-Image Pre-training (CLIP, [54]) and Large Language Models (LLMs, [5]) to automatically generate concept labels for each image ([50, 81, 37]).

Despite these advances, such approaches still achieve lower prediction performance than standard image models. Moreover, concept annotations produced by multimodal models such as CLIP can be unreliable and may fail to accurately capture underlying semantic concepts of individual images ([80, 30]).

3 Heavy-Tailed Activation Function and its application

3.1 Notation

For a given positive integer p , we denote $\{1, \dots, p\}$ as $[p]$. Let \mathbb{R}_+ denote the set of positive real numbers. For a given input $x \in \mathbb{R}$, we let $\sigma(\cdot)$ and $\psi(\cdot)$ as the sigmoid and hyperbolic tangent functions, respectively, i.e.,

$$\sigma(x) := \frac{1}{1 + \exp(-x)} \quad \text{and} \quad \psi(x) := \frac{\exp(x) - \exp(-x)}{\exp(x) + \exp(-x)}.$$

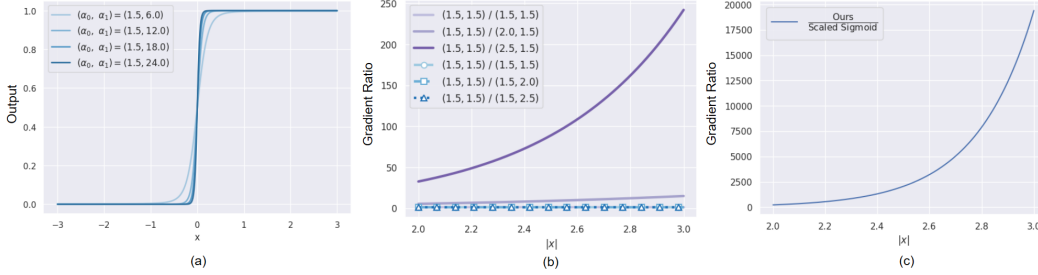


Figure 1: **Outputs and gradients of HTAF.** (a) Output curves of HTAF with fixed $\alpha_0 = 1.5$ and varying $\alpha_1 \in \{6.0, 12.0, 18.0, 24.0\}$. (b) Ratios of gradients relative to the baseline case $\alpha_0 = \alpha_1 = 1.5$, obtained by varying α_0 with α_1 fixed at 1.5 and varying α_1 with α_0 fixed at 1.5. Blue curves correspond to varying α_1 , while purple curves correspond to varying α_0 . (c) Ratio of derivatives between HTAF and Scaled Sigmoid in the tail region.

3.2 Heavy-Tailed Activation Function

For a given input $x \in \mathbb{R}$, we define Heavy-Tailed Activation Function (HTAF) as

$$\text{HTAF}(x|\alpha_0, \alpha_1) := \sigma(\alpha_1 \psi(\alpha_0 x)), \quad (1)$$

where $\alpha_0 \in \mathbb{R}_+$ and $\alpha_1 \in \mathbb{R}_+$ are hyperparameters.

HTAF has two key properties. First, it induces binarized (near-binary) outputs, i.e., $\text{HTAF}(x|\alpha_0, \alpha_1) \approx 0$ or 1 for all $x \in \mathbb{R}$ with an appropriate choice of α_0 and α_1 , as shown in Figure 1. Second, its gradient decays slowly in the tail regions while maintaining a large gradient magnitude around $x = 0$, ensuring stable gradient flow even for large input magnitudes while still closely approximating the Heaviside function. Due to these properties, HTAF enables stable learning of binary representations using a standard gradient descent algorithm. In the following, we describe these two properties in detail.

Proposition 3.1. For any $\epsilon \in (0, 1/2)$, suppose that α_0 and α_1 satisfy

$$\alpha_1 > \log\left(\frac{1-\epsilon}{\epsilon}\right) \quad \text{and} \quad \alpha_0 \geq \frac{1}{2\epsilon} \log\left(\frac{\alpha_1 + \log\left(\frac{1-\epsilon}{\epsilon}\right)}{\alpha_1 - \log\left(\frac{1-\epsilon}{\epsilon}\right)}\right).$$

Then, we have

$$\sup_{x \geq \epsilon} |1 - \text{HTAF}(x|\alpha_0, \alpha_1)| \leq \epsilon \quad \text{and} \quad \sup_{x \leq -\epsilon} |\text{HTAF}(x|\alpha_0, \alpha_1)| \leq \epsilon. \quad (2)$$

Proposition 3.1 presents the explicit sufficient conditions on the parameters α_0 and α_1 under which HTAF uniformly approximates the Heaviside function outside an arbitrarily small neighborhood of the origin. In particular, for any prescribed accuracy $\epsilon \in (0, 1/2)$, choosing α_0 and α_1 according to the stated bounds guarantees that HTAF is within ϵ of the Heaviside function on $(-\infty, -\epsilon] \cup [\epsilon, \infty)$.

Based on Proposition 3.1, we next discuss how to select the parameters α_0 and α_1 in practice. Figure 2 illustrates the lower bounds of α_0 and the product of α_1 and the lower bound of α_0 as functions of α_1 for $\epsilon = 0.1$. Furthermore, we observe that the product of α_1 and the lower bound of α_0 converges to 22 as α_1 increases. Therefore, one may consider choosing a small α_0 and a large α_1 while satisfying the condition $\alpha_0 \alpha_1 = 22$. See Appendix F.1 for an ablation study on this choice.

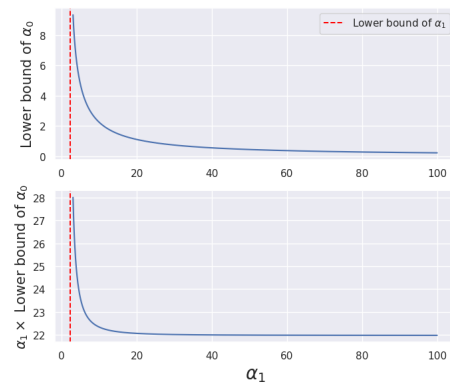


Figure 2: **Plots of the lower bound of α_0 and α_1 times the lower bound of α_0 as functions of α_1 for $\epsilon = 0.1$.**

An important message of Proposition 3.1 is that a neural network with the Heaviside activation function can be approximated by a DNN with HTAF activation with $O(\epsilon)$ approximation error where the constant term in $O(\epsilon)$ depends on the architecture of the neural network (i.e. the number of layers and number of nodes). See Appendix C for a theoretical justification.

We now study the gradient behavior of the proposed HTAF. The gradient of HTAF can exhibit a heavy-tailed behavior: that is, it decays slowly for large-magnitude inputs while maintaining a large magnitude near zero. This property is crucial for preventing premature gradient vanishing when approximating the Heaviside function. The following theorem summarizes this nice property of HTAF.

Theorem 3.2. *For any $\alpha_0 \in \mathbb{R}_+$ and $\alpha_1 \in \mathbb{R}_+$, we have the following:*

(a) *For large $|x|$, we have*

$$\frac{\partial HTAF(x|\alpha_0, \alpha_1)}{\partial x} = C(\alpha_0, \alpha_1) \exp(-2\alpha_0|x|),$$

where $C(\alpha_0, \alpha_1)$ is a constant that depends only on α_0 and α_1 .

(b) *We have*

$$\left. \frac{\partial HTAF(x|\alpha_0, \alpha_1)}{\partial x} \right|_{x=0} = \frac{\alpha_0 \alpha_1}{4}.$$

Theorem 3.2 - (a) implies that, in the tail region, the gradient of HTAF is governed mostly by α_0 . In Figure 1-(b), we observe that as α_0 increases, the gradient in the tail region decreases. On the other hand, Theorem 3.2-(b) implies that the slope of HTAF at the origin is determined by the product of the parameters α_0 and α_1 . This result implies that we can slow down the gradient decay by choosing a small α_0 , while maintaining a large gradient magnitude at zero by choosing a sufficiently large α_1 such that $\alpha_0 \alpha_1$ remains large. To sum up, from (a) and (b) of Theorem 3.2, it follows that when α_0 is chosen to be small but α_1 to be sufficiently large, HTAF maintains a sufficiently large gradient near zero while alleviating gradient vanishing in the tail regions.

We compare the gradient behavior of HTAF with that of Scaled Sigmoid (SS), which is defined as $\sigma_{\beta_0}(x) := \sigma(\beta_0 x)$. The parameters are set to be $\alpha_0 = 1.5$, $\alpha_1 = 5.0$, and $\beta_0 = 7.5$, ensuring that both functions have identical derivatives at $x = 0$. Figure 1-(c) presents the ratio of the HTAF derivative magnitude to the SS derivative magnitude in the tail regions, $|x| \in [2, 3]$. The result clearly shows that the gradient of HTAF is much larger than that of SS in the tail regions.

Theorem 3.2 suggests that choosing a small α_0 and large α_1 reduces gradient vanishing (See Appendix F.2.1). However, an excessively small α_0 may cause numerical issues, because maintaining a large gradient of HTAF at zero requires an excessively large α_1 , which can make the gradient of HTAF numerically unstable and effectively vanish. The results of numerical studies for the choice of α_0 and α_1 , which are presented in Appendix F.1, suggest that extremely small values of α_0 or extremely large values of α_1 should be avoided, as they can lead to unstable training.

Applicability as a general-purpose activation function. Although HTAF is designed to approximate the Heaviside function, it can also replace smooth activations such as sigmoid and ReLU. In particular, a DNN with HTAF achieves a near-minimax optimal convergence rate for smooth target functions when $\log(\alpha_0 \alpha_1)$ is bounded; see Appendix B. It is known that DHNs have inferior approximation properties for smooth target functions compared to standard DNNs with smooth activations ([34]). Surprisingly, however, DNNs with HTAF perform well at approximating both smooth functions and DHNs. One possible explanation is that the degree to which DNNs with HTAF activations approximate DHNs depends on the network architecture (e.g., the number of layers and the number of nodes per layer), which may lead to different asymptotic behaviors. This issue would be beyond the scope of this paper, and we leave it for future work.

3.3 Applications

3.3.1 Training Neural Networks with the Heaviside activation function

While Heaviside activation functions enable binary representations that are computationally efficient during inference, they preclude the direct use of gradient-based optimization because their gradients

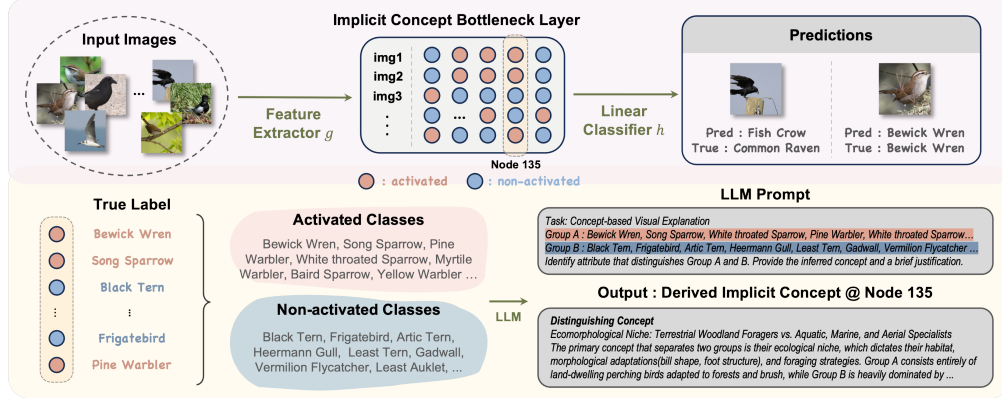


Figure 3: Overview of Implicit Concept Bottleneck Models.

are zero everywhere. Existing approaches therefore often rely on surrogate gradients, which introduce a mismatch between the forward and backward passes, or on smooth activation-based approximations that remain susceptible to gradient vanishing.

The first application of HTAF is surrogate-free training of neural networks with the Heaviside activation function, including SNNs, BNNs, and DHNs. Specifically, we replace each Heaviside activation functions with HTAF during training, allowing the network to be optimized using a standard gradient descent algorithm. After training, HTAF is replaced by the Heaviside function at the inference phase. This procedure preserves the learned weights and produces exact discrete activations, allowing the resulting model to benefit from the memory and computational efficiency of Heaviside-based inference without losing accuracy much.

3.3.2 Implicit Concept Bottleneck Models

Existing CBMs typically rely on either human-annotated or AI-annotated concepts. Human annotation is costly and labor-intensive, while AI-generated annotations can be unreliable. We propose a new approach to obtaining concepts for CBMs: instead of first asking an AI system to define or annotate concepts, we first learn concepts directly from data and then ask AI to interpret their meanings. This allows us to obtain concepts that are naturally relevant to the final prediction task. We refer to these data-driven concepts as implicit concepts. For implicit concepts to be desirable, we require them to satisfy the following properties:

1. **Binarity**: implicit concepts should be binary, indicating the presence or absence of a given concept.
2. **Class specificity**: implicit concepts should be class-specific; that is, for images belonging to the same class, each implicit concept should tend to be consistently activated or deactivated.
3. **Completeness**: implicit concepts should be complete, in the sense that predictions made solely from implicit concepts should not suffer from a significant loss in accuracy.

We propose Implicit Concept Bottleneck Models (ICBMs) to estimate implicit concepts. To be more specific, consider an arbitrary image classification model f , which can be decomposed into a feature extractor g and a linear classifier h , i.e., $f(\mathbf{x}) = h(g(\mathbf{x}))$, where \mathbf{x} is an input image. We define ICBM as a class of models where the activation function in the final layer of g is replaced with HTAF during training to approximate the Heaviside function, and with the Heaviside function at inference to produce exact binary outputs. In this way, g estimates implicit concepts. Because HTAF enables stable training of ICBM with gradient-based optimization, ICBM retains prediction performance comparable to, or better than, that of conventional image models, as shown in Section 4.2.1.

We now describe how each implicit concept can be interpreted once it is estimated by ICBMs. Since each concept is class-specific, we divide the class labels into two groups—one for activation and the other for non-activation. We then ask an LLM to explain a key feature that distinguishes these two groups. If there are pre-defined concept candidates provided by domain experts or learned automatically from data ([18]), we can ask an LLM to select one from the candidates or to generate a

new concept. The resulting description can be interpreted as the semantic meaning of a given implicit concept. An overview of ICBMs is presented in Figure 3.

Compared to CBM ([32]), ICBM has the following advantages. First, ICBM does not require annotated concept labels for images, making it applicable to a much broader range of datasets. Second, despite imposing this discrete bottleneck, ICBM does not suffer from a degradation in prediction performance, suggesting that the learned implicit concepts are complete. Our empirical results in Section 4.2.2 further show that the implicit concepts learned by ICBM are also class-specific.

4 Experiments

Comprehensive experimental results across a wide range of settings and tasks, along with ablation studies, applications to Large Language Models, and detailed descriptions of datasets, learning algorithms, and hyperparameter selection, are provided in Appendices D to G.

4.1 Deep Neural Networks with the Heaviside activation function

We compare the prediction performance of SNNs, BNNs and DHNs using STE, HTAF and SS. When using HTAF or SS, all Heaviside activation functions are replaced with these functions during training and reverted to the Heaviside function at inference. For STE method, the backward gradients are computed using a smooth surrogate function during training. For each model, we adopt backbone architectures as follows: Spiking Element-Wise ResNet (SEW-ResNet, [16]) for SNNs, Bi-Real Net ([42]) for BNNs, and WideResNet ([82]) for DHNs. Table 1 shows the average prediction accuracy over five runs on CIFAR-10 and CIFAR-100 datasets for all models.

Table 1: **Classification accuracies (%) on CIFAR-10 and CIFAR-100 for SNNs, BNNs and DHNs.**

Model	Dataset	HTAF	STE	SS
SNN	CIFAR-10	91.0%	91.2%	90.6%
	CIFAR-100	66.9%	63.9%	66.2%
BNN	CIFAR-10	75.8%	75.3%	60.6%
	CIFAR-100	46.1%	45.2%	31.3%
DHN	CIFAR-10	88.6%	83.3%	74.5%
	CIFAR-100	57.6%	56.7%	45.6%

These results indicate that HTAF achieves prediction performance competitive with STE in learning SNNs, while consistently outperforming both STE and SS in BNNs and DHNs. Overall, SS exhibits relatively poor performance in BNNs and DHNs, which is likely attributable to the gradient vanishing problem. Empirical evidence supporting this observation is provided in Appendix F.2.2.

Note that HTAF requires no special optimization techniques beyond standard gradient-based optimization. These results demonstrate the practical effectiveness of HTAF for training neural networks with Heaviside activation functions. Additional experiments including comparison ANN-to-SNN method are in Appendix E and the details of the experiments are in Appendix D.

4.2 Implicit Concept Bottleneck Models

Table 2: **Results of the average prediction accuracy with and without HTAF (i.e., using identity or ReLU) at the final layer of the feature extractor.**

Dataset	ResNet+ HTAF	ResNet	WideResNet+ HTAF	WideResNet	ViT+ HTAF	ViT
CIFAR-10	94.6%	94.6%	96.1%	95.7%	96.6%	96.7%
CIFAR-100	80.8%	80.0%	79.5%	78.2%	89.0%	88.6%
CUB-200	74.8%	74.5%	77.3%	77.5%	88.5%	87.1%
TINY IMAGENET	72.2%	72.1%	85.4%	85.7%	86.6%	86.7%

4.2.1 Prediction performance

In this section, we empirically demonstrate that HTAF can be effectively incorporated into various image classification models. We consider ResNet ([22]), WideResNet ([82]), and ViT [13] as backbone image models. We compare the prediction performance of the ICBM versions of these models to that of their original counterparts. Here, the ICBM version refers to a model trained by replacing

the activation function at the final layer of the feature extractor with HTAF, and evaluated at inference by replacing HTAF with the Heaviside function.

Table 2 presents the average prediction accuracy over five trials for various architectures on CIFAR-10, CIFAR-100, CUB-200, and TINY-IMAGENET datasets. Surprisingly, replacing the activation function in the last layer of the feature extractor with HTAF does not degrade prediction performance, even though the feature vectors are binary during inference. In particular, on CIFAR-100 and CUB-200 datasets, we observe that applying HTAF even leads to improved prediction performance. These results support that the implicit concepts estimated by ICBM are complete. Note that CBMs ([50, 81, 68]) typically suffer from degraded performance compared to conventional image models. Results of comparisons with other CBMs are provided in Appendix G.7.

4.2.2 Evaluating class specificity of implicit concepts

In this section, we evaluate whether implicit concepts are class-specific. That is, we examine whether the activation values on each node are consistently either 0 or 1 for images belonging to the same class. We use WideResNet as the backbone model and conduct experiments on CIFAR-10 dataset.

For images of the ‘Deer’ class, we compute, for each node, the proportion of outputs equal to one. As a baseline, we consider the original WideResNet and apply post hoc binarization to its activation values, converting them to zero or one. The binarization threshold for each node is chosen to match the proportion of zeros and ones to those observed in ICBM.

Figure 4 shows the histograms of these proportions for all methods on the ‘Deer’ class. Our method exhibits strong concentration near 0 and 1, whereas the baseline does not. This indicates that the implicit concepts learned by ICBM are activated in a class-specific manner. Additional results for other classes are in Appendix G.3.

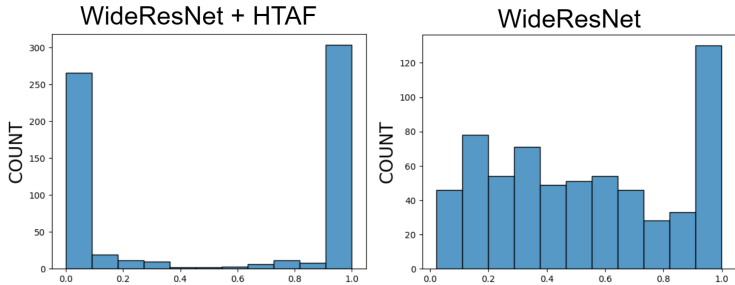


Figure 4: Histograms of the proportions for the ‘Deer’ class.

4.2.3 Interpretation

In this section, we illustrate how the learned implicit concepts can be interpreted using an LLM on CUB-200 dataset with the ViT model. For the *Bewick’s Wren* class, the top five important nodes based on the importance scores defined in Appendix G.2 are the 135th, 186th, 690th, 153rd, and 217th nodes. We analyze the semantic meaning of these nodes.

Figure 5a provides a visualization of the semantic properties captured by the 135th node in the final layer of the feature extractor. The upper row shows representative images from the activated group, corresponding to samples with activation value one, while the lower row shows those from the unactivated group, corresponding to samples with activation value zero.

We identify the implicit concept associated with the 135th node using the following steps. First, we collect the class labels of images that activate the node and those that do not, forming two groups. We then ask an LLM to explain distinguishing features between these two groups. Specifically, we compile two class-name lists and ask the LLM to infer semantic meanings of the corresponding implicit concept using the following prompt. The LLM’s responses are provided in Appendix G.1.

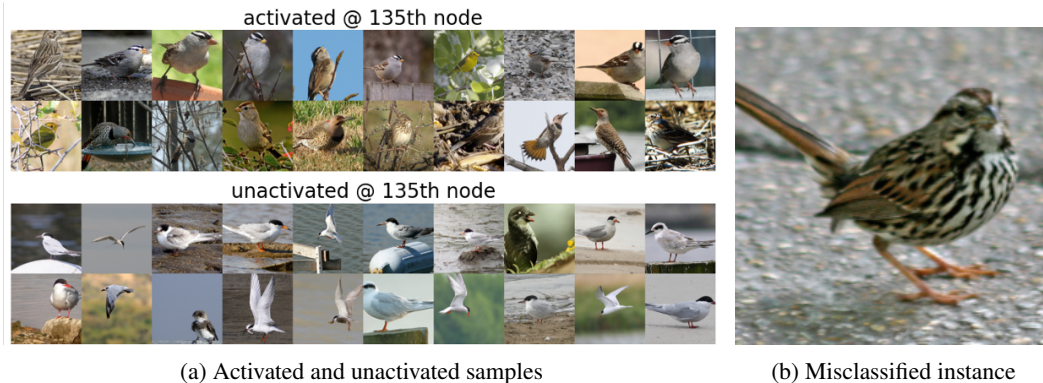


Figure 5: **Visual analysis of embedding space.** (a) The selected 20 images, showing activation value one (top) and zero (bottom) at the 135th node. (b) an image of *Bewick Wren* which is misclassified.

Prompt

Task: Concept-based Visual Explanation

Group A: [Names of classes whose constituent images have an activation value of 1 at the node]
 Group B: [Names of classes whose constituent images have an activation value of 0 at the node]

Identify the attribute that distinguishes Group A from Group B based on the two class lists.
 Provide the inferred concept and a brief justification.

In response to the prompt, the LLM identifies the underlying concept of the node as ‘*Ecomorphological Niche: Terrestrial Woodland Foragers vs. Aquatic, Marine, and Aerial Specialists*’. This result is highly consistent with Figure 5a. Notably, although the LLM is provided solely with textual class labels, the resulting explanation demonstrates a strong alignment with the visual characteristics of the actual images. We repeat this process for the other 4 nodes and obtain the results shown in Table 3.

Table 3: **Results of the estimated implicit concepts for top five important nodes.**

Node index	Estimated implicit concept	Label	Importance score
135	Ecomorphological Niche	0: Aquatic / 1: Terrestrial	0.1069
186	Bill Morphology	0: Stout or Conical / 1: Hooked or Spear-like	0.0941
690	Habitats	0: Dense Shrubland / 1: Open grassland	0.0922
153	Foraging mechanics	0: Extraction / 1: Snatching	0.0879
217	Visual Plumage Pigmentation	0: Yellow & Carotenoid / 1: Otherwise	0.0840

We now investigate why a certain image is misclassified. While most *Bewick’s Wren* images are correctly classified, the one shown in Figure 5b is misclassified. For correctly classified images, activation values of the five most important nodes (135, 186, 690, 153, and 217) are (1, 1, 0, 0, 1), indicating that the implicit concepts associated with nodes 135, 186, and 217 are present, while those corresponding to nodes 690 and 153 are absent. In contrast, for the misclassified image in Figure 5b, ICBM predicts activation values for the important nodes as (1, 0, 1, 1, 0), where nodes 135, 690, and 153 are active, and the others are not. Visually, the bird appears to exhibit features such as ‘*stout and conical bill*’, ‘*open grassland*’, and ‘*yellow and carotenoid plumage*’. As a result, ICBM misclassifies the image.

5 Conclusion

We proposed *Heavy Tail Activation Function (HTAF)*, a novel activation function that stably approximates the Heaviside function under gradient-based optimization by preserving gradient magnitude. We theoretically show that HTAF enables DNNs with Heaviside activation functions to learn effectively while alleviating the gradient vanishing problem in tail regions.

Based on the properties of HTAF, we further showed that HTAF provides an effective way to train DNNs with the Heaviside activation function using a standard gradient descent algorithm, without

surrogate gradients, while significantly improving training stability and prediction performance. Furthermore, we introduced *Implicit Concept Bottleneck Models (ICBMs)*, which estimate implicit concepts using HTAF while maintaining prediction performance across various architectures and datasets.

Although tuning the parameters of HTAF can alleviate the gradient vanishing problem, it cannot eliminate it completely. Addressing this limitation remains an important direction for future research. In addition, an important direction for future work is to investigate principled methods for determining the number of concepts in ICBM, as well as the theoretical properties of DNNs employing HTAF.

References

- [1] Telco customer churn. kaggle, 2017. <https://www.kaggle.com/datasets/blastchar/telco-customer-churn/data>.
- [2] Fico heloc. FICO Explainable Learning Challenge, 2018. <https://community.fico.com/s/explainable-machine-learning-challenge>.
- [3] Yoshua Bengio, Nicholas Léonard, and Aaron Courville. Estimating or propagating gradients through stochastic neurons for conditional computation. *arXiv preprint arXiv:1308.3432*, 2013.
- [4] Garrett Bingham and Risto Miikkulainen. Efficient activation function optimization through surrogate modeling. *Advances in Neural Information Processing Systems*, 36:6634–6661, 2023.
- [5] Tom Brown, Benjamin Mann, Nick Ryder, Melanie Subbiah, Jared D Kaplan, Prafulla Dhariwal, Arvind Neelakantan, Pranav Shyam, Girish Sastry, Amanda Askell, et al. Language models are few-shot learners. *Advances in neural information processing systems*, 33:1877–1901, 2020.
- [6] Yongqiang Cao, Yang Chen, and Deepak Khosla. Spiking deep convolutional neural networks for energy-efficient object recognition. *International Journal of Computer Vision*, 113(1):54–66, 2015.
- [7] Zhangjie Cao, Mingsheng Long, Jianmin Wang, and Philip S Yu. Hashnet: Deep learning to hash by continuation. In *Proceedings of the IEEE international conference on computer vision*, pages 5608–5617, 2017.
- [8] Chao Chen, Chenghua Guo, Rufeng Chen, Guixiang Ma, Ming Zeng, Xiangwen Liao, Xi Zhang, and Sihong Xie. Training for stable explanation for free. *Advances in Neural Information Processing Systems*, 37:3421–3457, 2024.
- [9] Wenlin Chen and Hong Ge. Neural characteristic activation analysis and geometric parameterization for relu networks. *Advances in Neural Information Processing Systems*, 37:97562–97586, 2024.
- [10] Paulo Cortez, A. Cerdeira, F. Almeida, T. Matos, and J. Reis. Wine Quality. 2009. DOI: <https://doi.org/10.24432/C56S3T>.
- [11] Matthieu Courbariaux, Itay Hubara, Daniel Soudry, Ran El-Yaniv, and Yoshua Bengio. Binarized neural networks: Training deep neural networks with weights and activations constrained to +1 or -1. *arXiv preprint arXiv:1602.02830*, 2016.
- [12] Peter U Diehl, Daniel Neil, Jonathan Binas, Matthew Cook, Shih-Chii Liu, and Michael Pfeiffer. Fast-classifying, high-accuracy spiking deep networks through weight and threshold balancing. In *2015 International joint conference on neural networks (IJCNN)*, pages 1–8. iee, 2015.
- [13] Alexey Dosovitskiy. An image is worth 16x16 words: Transformers for image recognition at scale. *arXiv preprint arXiv:2010.11929*, 2020.
- [14] Tolga Ergen, Halil Ibrahim Gulluk, Jonathan Lacotte, and Mert Pilanci. Globally optimal training of neural networks with threshold activation functions. *arXiv preprint arXiv:2303.03382*, 2023.
- [15] Wei Fang, Yanqi Chen, Jianhao Ding, Zhaofei Yu, Timothée Masquelier, Ding Chen, Liwei Huang, Huihui Zhou, Guoqi Li, and Yonghong Tian. Spikingjelly: An open-source machine learning infrastructure platform for spike-based intelligence. *Science Advances*, 9(40):ead11480, 2023.

- [16] Wei Fang, Zhaofei Yu, Yanqi Chen, Tiejun Huang, Timothée Masquelier, and Yonghong Tian. Deep residual learning in spiking neural networks. *Advances in neural information processing systems*, 34:21056–21069, 2021.
- [17] Thomas Fel, Agustin Picard, Louis Bethune, Thibaut Boissin, David Vigouroux, Julien Colin, Rémi Cadène, and Thomas Serre. Craft: Concept recursive activation factorization for explainability. In *Proceedings of the IEEE/CVF Conference on Computer Vision and Pattern Recognition*, pages 2711–2721, 2023.
- [18] Amirata Ghorbani, James Wexler, James Y Zou, and Been Kim. Towards automatic concept-based explanations. *Advances in neural information processing systems*, 32, 2019.
- [19] Xavier Glorot and Yoshua Bengio. Understanding the difficulty of training deep feedforward neural networks. In *Proceedings of the thirteenth international conference on artificial intelligence and statistics*, pages 249–256. JMLR Workshop and Conference Proceedings, 2010.
- [20] Xavier Glorot, Antoine Bordes, and Yoshua Bengio. Deep sparse rectifier neural networks. In *Proceedings of the fourteenth international conference on artificial intelligence and statistics*, pages 315–323. JMLR Workshop and Conference Proceedings, 2011.
- [21] Soufiane Hayou, Arnaud Doucet, and Judith Rousseau. On the impact of the activation function on deep neural networks training. In *International conference on machine learning*, pages 2672–2680. PMLR, 2019.
- [22] Kaiming He, Xiangyu Zhang, Shaoqing Ren, and Jian Sun. Deep residual learning for image recognition. In *Proceedings of the IEEE conference on computer vision and pattern recognition*, pages 770–778, 2016.
- [23] Dan Hendrycks, Norman Mu, Ekin D Cubuk, Barret Zoph, Justin Gilmer, and Balaji Lakshminarayanan. Augmix: A simple data processing method to improve robustness and uncertainty. *arXiv preprint arXiv:1912.02781*, 2019.
- [24] Edward J Hu, Yelong Shen, Phillip Wallis, Zeyuan Allen-Zhu, Yuanzhi Li, Shean Wang, Liang Wang, Weizhu Chen, et al. Lora: Low-rank adaptation of large language models. *Iclr*, 1(2):3, 2022.
- [25] Wei Huang, Yangdong Liu, Haotong Qin, Ying Li, Shiming Zhang, Xianglong Liu, Michele Magno, and Xiaojuan Qi. Billm: Pushing the limit of post-training quantization for llms. *arXiv preprint arXiv:2402.04291*, 2024.
- [26] Itay Hubara, Matthieu Courbariaux, Daniel Soudry, Ran El-Yaniv, and Yoshua Bengio. Quantized neural networks: Training neural networks with low precision weights and activations. *journal of machine learning research*, 18(187):1–30, 2018.
- [27] Shayan Hundrieser, Philipp Tüchel, Insung Kong, and Johannes Schmidt-Hieber. On the universal representation property of spiking neural networks. *arXiv preprint arXiv:2512.16872*, 2025.
- [28] A Iliev, Nikolay Kyurkchiev, and Svetoslav Markov. On the approximation of the step function by some sigmoid functions. *Mathematics and Computers in Simulation*, 133:223–234, 2017.
- [29] Yuling Jiao, Guohao Shen, Yuanyuan Lin, and Jian Huang. Deep nonparametric regression on approximate manifolds: Nonasymptotic error bounds with polynomial prefactors. *The Annals of Statistics*, 51(2):691–716, 2023.
- [30] Rémi Kazmierczak, Steve Azzolin, Eloïse Berthier, Goran Frehse, and Gianni Franchi. Enhancing concept localization in clip-based concept bottleneck models. *arXiv preprint arXiv:2510.07115*, 2025.
- [31] Been Kim, Martin Wattenberg, Justin Gilmer, Carrie Cai, James Wexler, Fernanda Viegas, et al. Interpretability beyond feature attribution: Quantitative testing with concept activation vectors (tcav). In *International conference on machine learning*, pages 2668–2677. PMLR, 2018.

- [32] Pang Wei Koh, Thao Nguyen, Yew Siang Tang, Stephen Mussmann, Emma Pierson, Been Kim, and Percy Liang. Concept bottleneck models. In *International conference on machine learning*, pages 5338–5348. PMLR, 2020.
- [33] Michael Kohler and Sophie Langer. On the rate of convergence of fully connected deep neural network regression estimates. *The Annals of Statistics*, 49(4):2231 – 2249, 2021.
- [34] Insung Kong, Juntong Chen, Sophie Langer, and Johannes Schmidt-Hieber. On the expressivity of deep heaviside networks. *arXiv preprint arXiv:2505.00110*, 2025.
- [35] Insung Kong and Yongdai Kim. Posterior concentrations of fully-connected bayesian neural networks with general priors on the weights. *Journal of Machine Learning Research*, 26(94):1–60, 2025.
- [36] Alex Krizhevsky, Geoffrey Hinton, et al. Learning multiple layers of features from tiny images. 2009.
- [37] Akshay Kulkarni, Ge Yan, Chung-En Sun, Tuomas Oikarinen, and Tsui-Wei Weng. Interpretable generative models through post-hoc concept bottlenecks. In *Proceedings of the Computer Vision and Pattern Recognition Conference*, pages 8162–8171, 2025.
- [38] Fayez Lahoud, Radhakrishna Achanta, Pablo Márquez-Neila, and Sabine Süsstrunk. Self-binarizing networks. *arXiv preprint arXiv:1902.00730*, 2019.
- [39] Yann Le and Xuan Yang. Tiny imagenet visual recognition challenge. *CS 231N*, 7(7):3, 2015.
- [40] Benjamin Leblanc and Pascal Germain. Seeking interpretability and explainability in binary activated neural networks. In *World Conference on Explainable Artificial Intelligence*, pages 3–20. Springer, 2024.
- [41] Yuhang Li, Yufei Guo, Shanghang Zhang, Shikuang Deng, Yongqing Hai, and Shi Gu. Differentiable spike: Rethinking gradient-descent for training spiking neural networks. *Advances in neural information processing systems*, 34:23426–23439, 2021.
- [42] Zechun Liu, Baoyuan Wu, Wenhan Luo, Xin Yang, Wei Liu, and Kwang-Ting Cheng. Bi-real net: Enhancing the performance of 1-bit cnns with improved representational capability and advanced training algorithm. In *Proceedings of the European conference on computer vision (ECCV)*, pages 722–737, 2018.
- [43] Jianfeng Lu, Zuowei Shen, Haizhao Yang, and Shijun Zhang. Deep network approximation for smooth functions. *SIAM Journal on Mathematical Analysis*, 53(5):5465–5506, 2021.
- [44] Shuming Ma, Hongyu Wang, Lingxiao Ma, Lei Wang, Wenhui Wang, Shaohan Huang, Lifeng Dong, Ruiping Wang, Jilong Xue, and Furu Wei. The era of 1-bit llms: All large language models are in 1.58 bits. *arXiv preprint arXiv:2402.17764*, 1(4), 2024.
- [45] Wolfgang Maass. Networks of spiking neurons: the third generation of neural network models. *Neural networks*, 10(9):1659–1671, 1997.
- [46] TorchVision maintainers and contributors. Torchvision: Pytorch’s computer vision library. <https://github.com/pytorch/vision>, 2016.
- [47] Todor Mihaylov, Peter Clark, Tushar Khot, and Ashish Sabharwal. Can a suit of armor conduct electricity? a new dataset for open book question answering. In *Proceedings of the 2018 conference on empirical methods in natural language processing*, pages 2381–2391, 2018.
- [48] Emre O Neftci, Hesham Mostafa, and Friedemann Zenke. Surrogate gradient learning in spiking neural networks. *IEEE Signal Processing Magazine*, 36(6):51–63, 2019.
- [49] Ilsang Ohn and Yongdai Kim. Smooth function approximation by deep neural networks with general activation functions. *Entropy*, 21(7):627, 2019.
- [50] Tuomas Oikarinen, Subhro Das, Lam M Nguyen, and Tsui-Wei Weng. Label-free concept bottleneck models. *arXiv preprint arXiv:2304.06129*, 2023.

- [51] Philipp Petersen and Felix Voigtlaender. Optimal approximation of piecewise smooth functions using deep ReLU neural networks. *Neural Networks*, 108:296–330, 2018.
- [52] Haotong Qin, Ruihao Gong, Xianglong Liu, Xiao Bai, Jingkuan Song, and Nicu Sebe. Binary neural networks: A survey. *Pattern Recognition*, 105:107281, 2020.
- [53] Qwen Team. Qwen3.5: Towards native multimodal agents, February 2026.
- [54] Alec Radford, Jong Wook Kim, Chris Hallacy, Aditya Ramesh, Gabriel Goh, Sandhini Agarwal, Girish Sastry, Amanda Askell, Pamela Mishkin, Jack Clark, et al. Learning transferable visual models from natural language supervision. In *International conference on machine learning*, pages 8748–8763. PmLR, 2021.
- [55] Mohammad Rastegari, Vicente Ordonez, Joseph Redmon, and Ali Farhadi. Xnor-net: Imagenet classification using binary convolutional neural networks. In *European conference on computer vision*, pages 525–542. Springer, 2016.
- [56] Frank Rosenblatt. The perceptron: a probabilistic model for information storage and organization in the brain. *Psychological review*, 65(6):386, 1958.
- [57] Bodo Rueckauer, Iulia-Alexandra Lungu, Yuhuang Hu, Michael Pfeiffer, and Shih-Chii Liu. Conversion of continuous-valued deep networks to efficient event-driven networks for image classification. *Frontiers in neuroscience*, 11:682, 2017.
- [58] David E Rumelhart, Geoffrey E Hinton, and Ronald J Williams. Learning representations by back-propagating errors. *nature*, 323(6088):533–536, 1986.
- [59] Keisuke Sakaguchi, Ronan Le Bras, Chandra Bhagavatula, and Yejin Choi. Winogrande: An adversarial winograd schema challenge at scale. *Communications of the ACM*, 64(9):99–106, 2021.
- [60] Johannes Schmidt-Hieber. Deep relu network approximation of functions on a manifold. *arXiv preprint arXiv:1908.00695*, 2019.
- [61] Johannes Schmidt-Hieber. Nonparametric regression using deep neural networks with ReLU activation function. *The Annals of Statistics*, 48(4):1875 – 1897, 2020.
- [62] Abhronil Sengupta, Yuting Ye, Robert Wang, Chiao Liu, and Kaushik Roy. Going deeper in spiking neural networks: Vgg and residual architectures. *Frontiers in neuroscience*, 13:95, 2019.
- [63] Noam Shazeer. Glu variants improve transformer. *arXiv preprint arXiv:2002.05202*, 2020.
- [64] Aaditya Singh, Adam Fry, Adam Perelman, Adam Tart, Adi Ganesh, Ahmed El-Kishky, Aidan McLaughlin, Aiden Low, AJ Ostrow, Akhila Ananthram, et al. Openai gpt-5 system card. *arXiv preprint arXiv:2601.03267*, 2025.
- [65] Vasu Singla, Sahil Singla, Soheil Feizi, and David Jacobs. Low curvature activations reduce overfitting in adversarial training. In *Proceedings of the IEEE/CVF International Conference on Computer Vision*, pages 16423–16433, 2021.
- [66] Amirhossein Tavanaei, Masoud Ghodrati, Saeed Reza Kheradpisheh, Timothée Masquelier, and Anthony Maida. Deep learning in spiking neural networks. *Neural networks*, 111:47–63, 2019.
- [67] Hugo Touvron, Louis Martin, Kevin Stone, Peter Albert, Amjad Almahairi, Yasmine Babaei, Nikolay Bashlykov, Soumya Batra, Prajjwal Bhargava, Shruti Bhosale, et al. Llama 2: Open foundation and fine-tuned chat models. *arXiv preprint arXiv:2307.09288*, 2023.
- [68] Moritz Vandenhirtz, Sonia Laguna, Ričards Marcinkevičs, and Julia Vogt. Stochastic concept bottleneck models. *Advances in Neural Information Processing Systems*, 37:51787–51810, 2024.
- [69] C. Wah, S. Branson, P. Welinder, P. Perona, and S. Belongie. The caltech-ucsd birds-200-2011 dataset. Technical Report CNS-TR-2011-001, California Institute of Technology, 2011.

- [70] Hongyu Wang, Shuming Ma, Li Dong, Shaohan Huang, Huaijie Wang, Lingxiao Ma, Fan Yang, Ruiping Wang, Yi Wu, and Furu Wei. Bitnet: Scaling 1-bit transformers for large language models. *arXiv preprint arXiv:2310.11453*, 2023.
- [71] Qingcan Wang et al. Exponential convergence of the deep neural network approximation for analytic functions. *arXiv preprint arXiv:1807.00297*, 2018.
- [72] Nash Warwick, Sellers Tracy, Talbot Simon, Cawthorn Andrew, and Ford Wes. Abalone. UCI Machine Learning Repository, 1995. DOI: <https://doi.org/10.24432/C55C7W>.
- [73] Zhirong Wu, Dahua Lin, and Xiaoou Tang. Adjustable bounded rectifiers: Towards deep binary representations. *arXiv preprint arXiv:1511.06201*, 2015.
- [74] Cihang Xie, Mingxing Tan, Boqing Gong, Alan Yuille, and Quoc V Le. Smooth adversarial training. *arXiv preprint arXiv:2006.14536*, 2020.
- [75] Yunfei Yang and Ding-Xuan Zhou. Optimal rates of approximation by shallow ReLU^k neural networks and applications to nonparametric regression. *Constructive Approximation*, pages 1–32, 2024.
- [76] Dmitry Yarotsky. Error bounds for approximations with deep ReLU networks. *Neural Networks*, 94:103–114, 2017.
- [77] Penghang Yin, Jiancheng Lyu, Shuai Zhang, Stanley Osher, Yingyong Qi, and Jack Xin. Understanding straight-through estimator in training activation quantized neural nets. *arXiv preprint arXiv:1903.05662*, 2019.
- [78] Ansheng You, Xiangtai Li, Zhen Zhu, and Yunhai Tong. Torchcv: A pytorch-based framework for deep learning in computer vision. <https://github.com/donnyou/torchcv>, 2019.
- [79] Chang Yue and Niraj K Jha. Learning interpretable differentiable logic networks. *IEEE Transactions on Circuits and Systems for Artificial Intelligence*, 2024.
- [80] Mert Yuksekgonul, Federico Bianchi, Pratyusha Kalluri, Dan Jurafsky, and James Zou. When and why vision-language models behave like bags-of-words, and what to do about it? *arXiv preprint arXiv:2210.01936*, 2022.
- [81] Mert Yuksekgonul, Maggie Wang, and James Zou. Post-hoc concept bottleneck models. *arXiv preprint arXiv:2205.15480*, 2022.
- [82] Sergey Zagoruyko and Nikos Komodakis. Wide residual networks. *arXiv preprint arXiv:1605.07146*, 2016.
- [83] Friedemann Zenke and Surya Ganguli. Superspike: Supervised learning in multilayer spiking neural networks. *Neural computation*, 30(6):1514–1541, 2018.
- [84] Shijun Zhang, Jianfeng Lu, and Hongkai Zhao. Deep network approximation: Beyond relu to diverse activation functions. *Journal of Machine Learning Research*, 25(35):1–39, 2024.

Impact statement

This paper presents research aimed at advancing the field of Machine Learning. While our work may have broader societal implications, we do not identify any specific consequences that require particular discussion here.

A Proofs

A.1 Proof of Proposition 3.1

Case of $x \geq \epsilon$. Since

$$\sigma(z) \geq 1 - \epsilon \Leftrightarrow z \geq \log\left(\frac{1 - \epsilon}{\epsilon}\right)$$

and

$$\alpha_1 \psi(\alpha_0 x) = \alpha_1 \left(\frac{\exp(2\alpha_0 x) - 1}{\exp(2\alpha_0 x) + 1} \right),$$

it is sufficient to find ranges of α_0 and α_1 satisfying the followings:

$$\alpha_1 \left(\frac{\exp(2\alpha_0 x) - 1}{\exp(2\alpha_0 x) + 1} \right) \geq \log\left(\frac{1 - \epsilon}{\epsilon}\right). \quad (3)$$

(3) is satisfied whenever α_0 and α_1 satisfy the followings:

$$\alpha_1 > \log\left(\frac{1 - \epsilon}{\epsilon}\right) \quad \text{and} \quad \alpha_0 \geq \frac{1}{2\epsilon} \log\left(\frac{\alpha_1 + \log\left(\frac{1 - \epsilon}{\epsilon}\right)}{\alpha_1 - \log\left(\frac{1 - \epsilon}{\epsilon}\right)}\right).$$

Case of $x \leq -\epsilon$. The proof is identical to that of the case $x \geq \epsilon$ and is therefore omitted. □

A.2 Proof of Theorem 3.2

Proof of (a). Direct calculation yields that

$$\begin{aligned} \frac{\partial \text{HTAF}(x|\alpha_0, \alpha_1)}{\partial x} &= \alpha_1 \sigma(\alpha_1 \psi(\alpha_0 x)) (1 - \sigma(\alpha_1 \psi(\alpha_0 x))) \frac{\partial \psi(\alpha_0 x)}{\partial x} \\ &= \alpha_1 \sigma(\alpha_1 \psi(\alpha_0 x)) (1 - \sigma(\alpha_1 \psi(\alpha_0 x))) \left(\alpha_0 (1 - \{\psi(\alpha_0 x)\}^2) \right). \end{aligned}$$

That is, for large $|x|$, we have

$$\begin{aligned} \frac{\partial \text{HTAF}(x|\alpha_0, \alpha_1)}{\partial x} &= C(\alpha_0, \alpha_1) (1 - \{\psi(\alpha_0 x)\}^2) \\ &= C(\alpha_0, \alpha_1) \exp(-2\alpha_0 |x|) \end{aligned}$$

for some constant $C(\alpha_0, \alpha_1)$ that depends on α_0 and α_1 . □

Proof of (b). From proof of (a), we have

$$\left. \frac{\partial \text{HTAF}(x|\alpha_0, \alpha_1)}{\partial x} \right|_{x=0} = \frac{\alpha_0 \alpha_1}{4}.$$

□

B Theoretical properties of Deep Neural Networks with HTAF

In this section, we study the minimax optimality of DNNs with HTAF for regression tasks. Here, DNNs with HTAF refers to DNNs that uses HTAF as its activation function. We first introduce the notation used throughout this section.

B.1 Notations

Basic Notation. Let $\mathbf{m} = (m_1, \dots, m_d) \in \mathbb{N}_0^d$ be a multi-index, where $\mathbb{N}_0 := \mathbb{N} \cup \{0\}$. For a function $f : [0, 1]^d \rightarrow \mathbb{R}$, we define the sup-norm as $\|f\|_\infty := \sup_{\mathbf{x} \in [0, 1]^d} |f(\mathbf{x})|$ and for $1 \leq p < \infty$, we write $\|f\|_{p, \mu} := (\int_{\mathcal{X}} f(\mathbf{x})^p \mu(d\mathbf{x}))^{1/p}$. For a given vector $\mathbf{x} \in \mathbb{R}^d$, we denote the L_1 norm by $|\mathbf{x}|_1 := \sum_{1 \leq j \leq d} |x_j|$, the infinity norm by $|\mathbf{x}|_\infty := \max_{1 \leq j \leq d} |x_j|$ and the zero norm by $|\mathbf{x}|_0 := \sum_{j=1}^d \mathbb{I}(x_j \neq 0)$. For $\mathbf{m} \in \mathbb{N}_0^d$, the mixed partial derivative of order \mathbf{m} is defined as

$$\partial^{\mathbf{m}} f := \frac{\partial^{|\mathbf{m}|} f}{\partial x_1^{m_1} \dots \partial x_d^{m_d}}.$$

Finally, let \mathcal{C}_d^m denote the class of functions on $[0, 1]^d$ that are m times continuously differentiable. Here, the partial derivatives of order \mathbf{m} with $|\mathbf{m}| \leq m$ are continuous. We denote DNNs using the ReLU activation function as deep ReLU networks.

Definition of the Hölder space. For a smoothness $\beta > 0$, we write $\lfloor \beta \rfloor$ for the greatest integer less than β . The Hölder space \mathcal{H}_d^β is defined as

$$\mathcal{H}_d^\beta := \{f \in \mathcal{C}_d^{\lfloor \beta \rfloor} : \|f\|_{\mathcal{H}_d^\beta} < \infty\}, \quad (4)$$

where

$$\|f\|_{\mathcal{H}_d^\beta} := \sum_{\mathbf{m} \in \mathbb{N}_0^d : |\mathbf{m}| \leq \lfloor \beta \rfloor} \|\partial^{\mathbf{m}} f\|_\infty + \sum_{\mathbf{m} \in \mathbb{N}_0^d : |\mathbf{m}| = \lfloor \beta \rfloor} \sup_{\mathbf{x}_1, \mathbf{x}_2 \in [0, 1]^d, \mathbf{x}_1 \neq \mathbf{x}_2} \frac{|\partial^{\mathbf{m}} f(\mathbf{x}_1) - \partial^{\mathbf{m}} f(\mathbf{x}_2)|}{|\mathbf{x}_1 - \mathbf{x}_2|^{\beta - \lfloor \beta \rfloor}}. \quad (5)$$

For example, \mathcal{H}_d^1 corresponds to the space of bounded Lipschitz continuous functions. For $R > 0$, we defined the Hölder space $\mathcal{H}_d^\beta(R)$ as

$$\mathcal{H}_d^\beta(R) := \{f \in \mathcal{H}_d^\beta, \|f\|_{\mathcal{H}_d^\beta} \leq R\}. \quad (6)$$

Definition of DNNs with HTAF. Let $\text{HTAF}_{\alpha_0, \alpha_1} := \text{HTAF}(\cdot | \alpha_0, \alpha_1)$. A DNN with HTAF and $L \in \mathbb{N}$ layers, $n_\ell \in \mathbb{N}$ many nodes at the ℓ -th hidden layer for $\ell = 1, \dots, L$, input dimension $n_0 = d$, output dimension $n_{L+1} = 1$ and $\text{HTAF}_{\alpha_0, \alpha_1}$ is express as

$$f_{\theta, \alpha_0, \alpha_1}^{\text{HTAF}}(\mathbf{x}) := A_{L+1} \circ \text{HTAF}_{\alpha_0, \alpha_1} \circ A_L \circ \dots \circ A_2 \circ \text{HTAF}_{\alpha_0, \alpha_1} \circ A_1(\mathbf{x}), \quad (7)$$

where $A_\ell : \mathbb{R}^{n_{\ell-1}} \rightarrow \mathbb{R}^{n_\ell}$ is an affine map defined by $A_\ell(\mathbf{x}) = \mathbf{W}_\ell \mathbf{x} + \mathbf{b}_\ell$. Here, $\mathbf{W}_\ell \in \mathbb{R}^{n_\ell \times n_{\ell-1}}$ is a weight matrix and $\mathbf{b}_\ell \in \mathbb{R}^{n_\ell}$ is a bias vector. Let θ be the set of all parameters including weight matrices and bias vectors, i.e., $\theta := (\mathbf{W}_1, \mathbf{b}_1, \dots, \mathbf{W}_{L+1}, \mathbf{b}_{L+1})$. For a given parameter θ , let $L(\theta)$ denote the number of hidden layers (depth), and let $n_{\max}(\theta)$ denote the maximum number of hidden units per layer (width). Note that the zero norm and infinity norm of θ is expressed as

$$|\theta|_0 = \sum_{\ell=1}^{L+1} (|\text{vec}(\mathbf{W}_\ell)|_0 + |\mathbf{b}_\ell|_0), \quad (8)$$

$$|\theta|_\infty = \max \left\{ \max_{\ell \in [L+1]} |\text{vec}(\mathbf{W}_\ell)|_\infty, \max_{\ell \in [L+1]} |\mathbf{b}_\ell|_\infty \right\}, \quad (9)$$

where $\text{vec}(\mathbf{W}_\ell)$ denotes the vectorization of \mathbf{W}_ℓ obtained by concatenating its column vectors. Finally, we define the function spaces $\mathcal{F}_{\alpha_0, \alpha_1}(L, N)$ and $\mathcal{F}_{\alpha_0, \alpha_1}(L, N, S, B)$ of DNNs with HTAF by

$$\mathcal{F}_{\alpha_0, \alpha_1}(L, N) := \{f_{\theta, \alpha_0, \alpha_1}^{\text{HTAF}} : L(\theta) \leq L, n_{\max}(\theta) \leq N\}, \quad (10)$$

$$\mathcal{F}_{\alpha_0, \alpha_1}(L, N, S, B) := \{f_{\theta, \alpha_0, \alpha_1}^{\text{HTAF}} : L(\theta) \leq L, n_{\max}(\theta) \leq N, |\theta|_0 \leq S, |\theta|_\infty \leq B\}. \quad (11)$$

B.2 Expressivity

In this section, we investigate the expressive power of DNNs with HTAF. First, we show that DNNs with HTAF can approximate any deep ReLU networks with arbitrary precision, provided that the network is a constant factor larger.

Theorem B.1. *For any deep ReLU network f^{ReLU} with L hidden layers and N hidden units per layer, and any $\alpha_0, \alpha_1, \epsilon > 0$, there exists a DNN with HTAF*

$$f_{\theta, \alpha_0, \alpha_1}^{\text{HTAF}} \in \mathcal{F}_{\alpha_0, \alpha_1}(2L, 3N)$$

satisfying

$$\|f_{\theta, \alpha_0, \alpha_1}^{\text{HTAF}} - f^{\text{ReLU}}\|_{\infty} \leq \epsilon.$$

Proof. Since $\text{HTAF}_{\alpha_0, \alpha_1}$ is twice differentiable and non-affine, there exists $x_0 \in \mathbb{R}$ such that $\text{HTAF}_{\alpha_0, \alpha_1}^{(2)}(x_0) \neq 0$. We get the assertion by applying Theorem 1 of [84]. \square

The approximation capabilities of deep ReLU networks have been widely studied across various settings ([29, 33, 35, 43, 51, 60, 61, 71, 75, 76]). An implication of Theorem B.1 is that the expressivity properties of deep ReLU networks carry over directly to DNNs with HTAF.

Interestingly, DHNs, despite being well approximated by DNNs with HTAF with sufficiently large α_0 and α_1 , exhibit limited expressivity. For example, Theorem 1 of [34] shows that, for any non-constant target function, achieving an approximation error $\leq \epsilon$ requires the DHN to have at least $\gtrsim 1/\epsilon$ neurons in the first hidden layer, regardless of how deep the model is. On the other hand, combining Theorem B.1 with Theorem 6 of [71], it follows that for any analytic function f_0 , there exists a DNN with HTAF of depth $\lesssim \log^2(1/\epsilon)$ and constant width achieving an approximation error $\leq \epsilon$. This shows that DNNs with HTAF not only help train DHNs but can also serve as a proxy for them without suffering from limited expressivity.

Indeed, α_0 and α_1 neither affect the depth and width required to achieve a given approximation error nor influence the scale of the parameters. The following theorem provides such an example and will be used to derive the statistical convergence rate later.

Theorem B.2. *There exist positive constants L_0, N_0, S_0 and B_0 depending only on (d, β, R) , such that for any $f_0 \in \mathcal{H}_d^{\beta}(R)$ and $\epsilon > 0$, there exists a DNN with HTAF*

$$f_{\theta, \alpha_0, \alpha_1}^{\text{HTAF}} \in \mathcal{F}_{\alpha_0, \alpha_1}(L_0 \log(1/\epsilon), N_0 \epsilon^{-d/\beta}, S_0 \epsilon^{-d/\beta}, B_0 \epsilon^{-4(d/\beta+1)})$$

satisfying

$$\|f_{\theta, \alpha_0, \alpha_1}^{\text{HTAF}} - f_0\|_{\infty} \leq \epsilon.$$

Proof. We apply Theorem 1 of [49], keeping track of the dependence of the implicit constants on α_0 and α_1 . It suffices to consider the construction of the square function $x \mapsto x^2$ (Lemma A3.(a) of [49]), as the remaining part of the proof depends only on this structure.

Suppose that an activation function ϕ is three times continuously differentiable. Additionally, assume that there exists an interval (a, b) on which ϕ has bounded derivatives up to order three, and that there exists $t \in (a, b)$ such that both $\phi'(t)$ and $\phi''(t)$ are non-zero. For sufficiently large K with $\min(t - a, b - t) > 2/K$, [49] considered a deep neural network with 1 hidden layer, 3 hidden neurons and the activation function ϕ ,

$$f_{\phi}(x) := \sum_{k=0}^2 (-1)^{k-1} \frac{K^2}{\phi''(t)} \binom{2}{k} \phi\left(\frac{k}{K}x + t\right). \quad (12)$$

Then, it holds for some constant $c > 0$,

$$\sup_{x \in [0, 1]} |f_{\phi}(x) - x^2| \leq c \frac{\sup_{z \in (a, b)} |\phi'''(z)|}{K |\phi''(t)|}. \quad (13)$$

For $s \in [0, 1]$, define

$$u := \psi(\alpha_0 s), \quad p := \sigma(\alpha_1 u) = \text{HTAF}(s | \alpha_0, \alpha_1).$$

Then, we have

$$\begin{aligned}\text{HTAF}^{(1)}(s|\alpha_0, \alpha_1) &= \alpha_0\alpha_1(1-u^2)p(1-p), \\ \text{HTAF}^{(2)}(s|\alpha_0, \alpha_1) &= \alpha_0^2\alpha_1(1-u^2)p(1-p)[-2u + \alpha_1(1-2p)(1-u^2)] \\ \text{HTAF}^{(3)}(s|\alpha_0, \alpha_1) &= \alpha_0^3\alpha_1(1-u^2)p(1-p)\left[6u^2 - 2 - 6\alpha_1u(1-2p)(1-u^2) \right. \\ &\quad \left. + \alpha_1^2(1-6p+6p^2)(1-u^2)^2\right].\end{aligned}$$

In particular, for any sufficiently large α_0 and α_1 , if we put $s = s_0 := \psi^{-1}(\alpha_1^{-1})/\alpha_0$, then $u = 1/\alpha_1$ and $p = (1 + e^{-1})^{-1}$. Hence,

$$\text{HTAF}^{(2)}\left(\frac{\psi^{-1}(\alpha_1^{-1})}{\alpha_0} \mid \alpha_0, \alpha_1\right) \gtrsim \alpha_0^2\alpha_1^2.$$

On the other hand, as both $\psi(\cdot)$ and σ are bounded function, we have $\text{HTAF}^{(3)}(x|\alpha_0, \alpha_1) \lesssim \alpha_0^3\alpha_1^3$.

We plug in $\phi = \text{HTAF}_{\alpha_0, \alpha_1}$ and $t = s_0$ into (12) and (13). Then, for

$$f_{\xi, \alpha_0, \alpha_1}^{\text{HTAF}} := \sum_{k=0}^2 (-1)^{k-1} \frac{K^2}{\phi''(t)} \binom{2}{k} \phi\left(\frac{k}{K}x + s_0\right).$$

we get

$$\sup_{x \in [0, 1]} |f_{\xi, \alpha_0, \alpha_1}^{\text{HTAF}} - x^2| \lesssim \frac{\alpha_0\alpha_1}{K}.$$

Observe that the magnitudes of the parameters in $f_{\xi, \alpha_0, \alpha_1}^{\text{HTAF}}$ are bounded by $O(K^2/(\alpha_0\alpha_1)^2)$. Recall that K can be chosen arbitrary large. By defining $M = K/(\alpha_0\alpha_1)$, we obtain that for any sufficiently large M , there exists $f_{\xi, \alpha_0, \alpha_1}^{\text{HTAF}}$ with $L(\xi) = 1$, $N(\xi) = 3$ and $|\xi|_\infty = O(M^2)$ such that

$$\sup_{x \in [0, 1]} |f_{\xi, \alpha_0, \alpha_1}^{\text{HTAF}} - x^2| \lesssim \frac{1}{M},$$

where the implicit constants do not depend on α_0 or α_1 . Hence, we recover the same conclusion as in Lemma A3.(a) of [49], and consequently the same assertion as in Theorem 1 of [49]. \square

B.3 Statistical convergence rate

In this section, we investigate statistical convergence rates of DNNs with HTAF in a nonparametric regression setting. Building upon the approximation results established in the previous section, we show that DNN estimators with HTAF achieves the near-minimax optimal convergence rate over the Hölder class, under mild assumptions on α_0 and α_1 . This result demonstrates that HTAF preserves not only the expressive power but also the statistical optimality of deep neural networks.

For a given f_0 , we consider a nonparametric regression model where the input variable \mathbf{X} follows a distribution $\mathbb{P}_{\mathbf{X}}$, and the response variable satisfies

$$Y|\mathbf{X} = \mathbf{x} \sim N(f_0(\mathbf{x}), 1). \quad (14)$$

Let $(\mathbf{X}_1, Y_1), \dots, (\mathbf{X}_n, Y_n)$ be independent copies of (\mathbf{X}, Y) . Theorem B.3 shows that the DNN estimators with HTAF achieves the minimax optimal rate, and that the dependence on α_0 and α_1 appears only through logarithmic factors.

Theorem B.3. *For any $\kappa, R, \alpha_0, \alpha_1 > 0$, there exist positive constants L_0, N_0, S_0 , and B_0 such that the DNN with HTAF estimator*

$$\hat{f}_n \in \arg \min_{f \in \mathcal{F}_n} \sum_{i=1}^n (Y_i - f(\mathbf{X}_i))^2$$

with

$$\mathcal{F}_n := \left\{ f_{\xi, \alpha_0, \alpha_1}^{\text{HTAF}} \in \mathcal{F}(L_0 \log n, N_0 n^{\frac{d}{2\beta+d}}, S_0 n^{\frac{d}{2\beta+d}} \log n, B_0 n^\kappa) : \|f_{\xi, \alpha_0, \alpha_1}^{\text{HTAF}}\|_\infty \leq 2R \right\}$$

satisfies

$$\sup_{f_0 \in \mathcal{H}_d^\beta(R)} \mathbb{E}_n \left[\| \hat{f}_n - f_0 \|_{2, \mathbb{P}_n}^2 \right] \leq C n^{-\frac{2\beta}{2\beta+d}} \left(\log^3 n + \log^2 n \log(\alpha_0 \alpha_1) \right)$$

for some constant $C > 0$.

Proof. Since $\text{HTAF}_{\alpha_0, \alpha_1}$ is $(\alpha_0 \alpha_1)$ -Lipschitz continuous, Proposition 1 of [49] yields

$$\log \mathcal{N} \left(\frac{1}{n}, \mathcal{F}_n, \|\cdot\|_\infty \right) \lesssim n^{\frac{d}{2\beta+d}} \left(\log^3 n + \log^2 n \log(\alpha_0 \alpha_1) \right). \quad (15)$$

We obtain the desired assertion by applying Lemma 4 of [61] together with Theorem B.2 and (15). \square

C Approximation of a DNN with the Heaviside activation function by a DNN with HTAF activation

In this section, we prove that a DNN can be approximated by a DNN with HTAF activation as long as the Heaviside function is well approximated by HTAF. For notational simplicity, we only consider a DNN with one hidden layer. The proof could be extended for multi-layer DNNs without much difficulty.

Let $\sigma_H(x)$ be the Heaviside function (i.e. $\sigma_H(x) = \mathbb{I}(x \geq 0)$). Let $f : \mathbb{R}^d \rightarrow \mathbb{R}$ be a DNN with the Heaviside activation function given as

$$f(\mathbf{x}) = W_1^\top \sigma_H(\mathbf{W}_0 \mathbf{x} + \mathbf{b}),$$

where W_1 is a n_1 dimensional vector, \mathbf{W} is an $n_1 \times d$ dimensional matrix and \mathbf{b} is an n_1 dimensional vector. Let $g(\mathbf{x})$ be the DNN obtained by replacing the Heaviside activation in f by HTAF activation. That is

$$g(\mathbf{x}) = W_1^\top \text{HTAF}(\mathbf{W}_0 \mathbf{x} + \mathbf{b} | \alpha_0, \alpha_1).$$

Let $h_j(\mathbf{x})$ be the j entry of $\mathbf{W}_0 \mathbf{x} + \mathbf{b}$ for $j = 1, \dots, n_1$.

Theorem C.1. *For given random vector $\mathbf{X} \sim \mathbb{P}_{\mathbf{X}}$, we assume the following regularity conditions:*

(C) *For $\epsilon \in (0, 1/2)$, there exists a constant $C > 0$ such that*

$$\mathbb{P}_{\mathbf{X}}\{|h_j(\mathbf{X})| \in (-\epsilon, \epsilon)\} \leq C\epsilon$$

for all $j \in [n_1]$.

Then, the following holds.

$$\mathbb{E}_{\mathbf{X}}[|f(\mathbf{X}) - g(\mathbf{X})|] \leq n_1 \|W_1\|_\infty (1 + C)\epsilon.$$

Proof. Suppose that α_0 and α_1 satisfies the conditions in Proposition 3.1. Then, we have

$$|f(\mathbf{x}) - g(\mathbf{x})| \leq \|W_1\|_\infty \sum_{j=1}^{n_1} |\sigma_H(h_j(\mathbf{x})) - \text{HTAF}(h_j(\mathbf{x}) | \alpha_0, \alpha_1)|.$$

Condition (C) and Proposition 3.1 imply that

$$\mathbb{E}_{\mathbf{X}}[|\sigma_H(h_j(\mathbf{x})) - \text{HTAF}(h_j(\mathbf{x}) | \alpha_0, \alpha_1)|] \leq (1 + C)\epsilon,$$

and thus we conclude that

$$\mathbb{E}_{\mathbf{X}}[|f(\mathbf{X}) - g(\mathbf{X})|] \leq n_1 \|W_1\|_\infty (1 + C)\epsilon.$$

□

Note that Condition (C) is mild and can be satisfied under reasonable assumptions on $\mathbb{P}_{\mathbf{X}}$, \mathbf{W}_0 , and \mathbf{b} .

D Details of the experiments

D.1 Data description

Table 4: Descriptions for datasets.

Dataset	Data size	# of feature	Type	Task
CIFAR-10 ([36])	60,000	–	Image	Classification
CIFAR-100 ([36])	60,000	–	Image	Classification
CUB-200 ([69])	11,788	–	Image	Classification
TINY-IMAGENET ([39])	100,000	–	Image	Classification
WINE ([10])	4,898	11	Tabular	Regression
ABALONE ([72])	4,178	8	Tabular	Regression
CHURN ([1])	7,043	20	Tabular	Classification
FICO ([2])	10,459	23	Tabular	Classification
WINOGRANDE-SMALL ([59])	1,907	–	Language	Classification
WINOGRANDE-MEDIUM ([59])	3,823	–	Language	Classification
OPENBOOKQA ([47])	5,456	–	Language	Classification

Table 4 presents the descriptions of the datasets used in our experiments.

D.2 Training details

We experiment with both Adam and SGD optimizers and report the best-performing configuration. The learning rate is selected via hyperparameter tuning from the candidate set $\{10^{-1}, 10^{-2}, 10^{-3}, 10^{-4}\}$. The batch size is set to the largest value that can be accommodated within the available computational resources. We standardize the image data independently for each RGB channel. Additionally, all images were distributed as train/test sets. The train set was further split into train/validation datasets: the train set was used for model training, the validation set for hyperparameter tuning, and the test set for evaluating the final prediction performance. For tabular data, we use min-max scaling for normalization.

D.3 Computational resources

All experiments were conducted using RTX 3090 and RTX 4090 GPUs with 24 GB VRAM, as well as RTX PRO 6000 GPUs with 96 GB VRAM.

D.4 Experimental Details for Deep Neural Networks with the Heaviside activation function

Details for Spiking Neural Networks experiments. We use Spike-Element-Wise (SEW) ResNet as the backbone SNN model and implement it with minor modifications based on the official code available at <https://github.com/fangwei123456/Spike-Element-Wise-ResNet>. For STE method, we consider multiple surrogate gradients, including the sigmoid, hyperbolic tangent, and rectangular functions, and report the best prediction performance among them. These surrogate gradients are defined as follows:

$$g_{\text{sigmoid}}(x) = \sigma(x) (1 - \sigma(x)), \quad g_{\text{tanh}}(x) = 1 - \tanh^2(x), \quad g_{\text{rect}}(x) = \begin{cases} 1 & \text{if } |x| < 1 \\ 0 & \text{otherwise} \end{cases} \quad (16)$$

For the parameters α_0 and α_1 in (1), we select the optimal values from the candidate set $\{(0.1, 220), (0.5, 44), (1, 22), (2, 11), (3, 7.3), (5, 4.4)\}$. For β_0 in Scaled Sigmoid, we select the optimal value from the candidate set $\{10, 22, 50, 100\}$.

Details for Binary Neural Networks experiments. We use Bi-Real Net ([42]) as the backbone BNN model, and implement it with minor modifications based on the official code provided in <https://github.com/liuzechun/Bi-Real-net>. For STE method, we use the same surrogate gradient as in [42]. For α_0, α_1 and β_0 , we select the optimal values from the candidate set in the SNN experiments.

Details for Deep Heaviside neural Networks experiments. We use WideResNet ([82]) as the backbone image model and implement it with minor modifications based on the official code available at <https://github.com/google-research/augmix>. For STE method, we use the same surrogate gradients as those considered in the SNN experiments. For α_0 , α_1 and β_0 , we choose optimal parameters from the candidate set in the experiment of SNNs.

D.5 Details for ICBM experiments

In this section, we describe the details of experiments for image datasets. For α_0 , α_1 and β_0 , we choose optimal parameters from the candidate set in Appendix D.4. We use GPT-5 ([64]) as a large language model to interpret the implicit concepts estimated by ICBM. The details of architectures for the backbone image models are summarized below.

ResNet. We use ResNet-18 architecture for all experiments, with different pretrained weights depending on the dataset. Specifically, for CIFAR-10, we use a model from https://huggingface.co/edadaltocg/ResNet18_cifar10; for CIFAR-100 and TINY-IMAGENET, we use models provided by [46]; and for CUB-200, we use a model from [78].

WideResNet. For CIFAR-10 and CIFAR-100, we use WideResNet models (WRN-40-6 and WRN-28-6), which are trained from scratch using the code provided in [23]. Here, WRN-40-6 denotes a WideResNet with depth 40 and widen factor 6, and WRN-28-6 is defined similarly. For CUB-200 and TINY-IMAGENET, we use an ImageNet-pretrained WideResNet-50 model from [46] and fine-tune it.

ViT. For CIFAR-10, CIFAR-100, CUB-200, and TINY-IMAGENET, we fine-tune a ViT-Base model with a patch size of 32×32 , initialized from the pretrained model provided at <https://huggingface.co/google/vit-base-patch32-224-in21k>.

E Comparison to ANN-to-SNN method

Table 5: Results of the prediction accuracy and inference time comparison between ANN-to-SNN conversion and our method.

Dataset	Metric	ANN-to-SNN					SNN with HTAF
		$T = 10$	$T = 30$	$T = 50$	$T = 100$	$T = 200$	$T = 4$
CIFAR-10	Accuracy	10.0%	93.4%	37.1%	81.0%	92.1%	91.0%
	Inference time	8 sec	27 sec	46 sec	85 sec	183 sec	3 sec
CIFAR-100	Accuracy	1.0%	3.5%	12.8%	47.8%	68.9%	66.9%
	Inference time	10 sec	25 sec	40 sec	81 sec	160 sec	3 sec

Here, we conduct experiments to compare our method with the ANN-to-SNN conversion method ([57]). We implement the ANN-to-SNN code from [15]. We use ResNet-18 as the backbone image model for ANN-to-SNN method and hyperparameters are turned as in Appendix D. A SNN with HTAF refers to a model that is trained by replacing the Heaviside activation function with HTAF, while at inference time, the activation function is reverted to the Heaviside function.

Table 5 presents the accuracy of the ANN-to-SNN method across different time steps T , along with the accuracy of SNNs with HTAF. Although ANN-to-SNN achieves higher accuracy at large time steps (e.g., $T=200$), this comes at a substantial cost in inference time, which increases by approximately 60 times. In contrast, our method maintains competitive accuracy with significantly fewer time steps (e.g., $T=4$), resulting in substantially efficiency inference.

F Additional experiments for Deep Heaviside neural Networks

F.1 Prediction performance analysis based on Proposition 3.1

In this section, we conduct experiments to evaluate the prediction performance of DNNs using HTAF as the activation function under the lower bounds of α_0 and α_1 in Proposition 3.1. The DNN architecture consists of three hidden layers with 256, 256, and 128 nodes, respectively. We use the Adam optimizer with a learning rate of 0.001 and train the model for 1,000 epochs. Experiments are conducted on CHURN dataset.

Recall that the lower bounds of α_0 and α_1 are given by

$$\alpha_1 > \log\left(\frac{1-\epsilon}{\epsilon}\right),$$

$$\alpha_0 \geq \frac{1}{2\epsilon} \log\left(\frac{\alpha_1 + \log\left(\frac{1-\epsilon}{\epsilon}\right)}{\alpha_1 - \log\left(\frac{1-\epsilon}{\epsilon}\right)}\right).$$

Specifically, for $\epsilon = 0.1$, the lower bound of α_1 is 2.20 and the corresponding lower bounds of α_0 for different values of α_1 are reported in Table 6. Figure 6 presents the AUROC and binarity score with respect to the lower bound of α_0 and the value of α_1 reported in Table 6. The definition of the binarity score is provided in Appendix G.4.

Theoretically, increasing α_1 and decreasing α_0 should improve prediction performance, as this leads to larger gradients in the tail region. However, empirical results show that while moderate adjustments can improve prediction performance, excessively large α_1 or overly small α_0 induce training instability and degrade prediction performance. Therefore, careful selection of α_0 and α_1 is required.

Table 6: Lower bounds of α_0 for different values of α_1 .

α_1 value	5	10	20	30	40	50	100	500	1000	5000
Lower bound of α_0	4.72	2.24	1.11	0.74	0.55	0.44	0.22	0.05	0.022	0.005

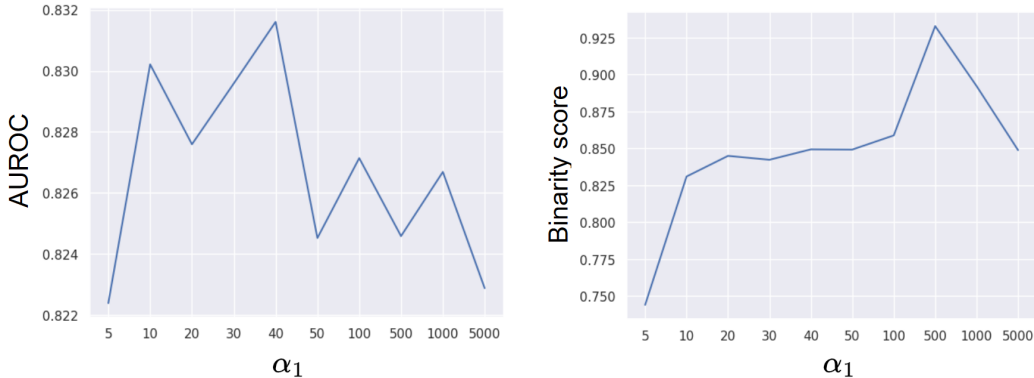


Figure 6: Plots of the AUROC and binarity score depends on various α_0 and α_1 .

F.2 Analysis of vanishing gradients

F.2.1 Mitigating gradient vanishing by reducing α_0

We aim to investigate whether gradient vanishing can be alleviated by reducing α_0 while keeping $\alpha_0\alpha_1$ fixed. The DNN architecture is set to [256, 256, 128], and β_0 is fixed at 22. We consider three candidates (2, 11), (8, 2.75), and (11, 2) for (α_0, α_1) . Experiments are conducted on ABALONE dataset.

We examine the gradients at each layer during training to investigate whether gradient vanishing occurs. Specifically, following [19], we compute the logarithm of the average L2 norm of the gradients of the loss with respect to the pre-activations at each layer over epochs. We also track the training loss over epochs.

Figure 7 presents results for a DNN architecture with hidden layer sizes (256, 256, 128) using HTAF, ReLU, and Scaled Sigmoid. Here, Batch normalization is not applied in these experiments.

While gradient vanishing is observed for Scaled Sigmoid and HTAF with (8, 2.75) and (11, 2), it is not observed for HTAF with (2, 11) and ReLU. This suggests that adjusting α_0 can resolve the vanishing gradient problem.

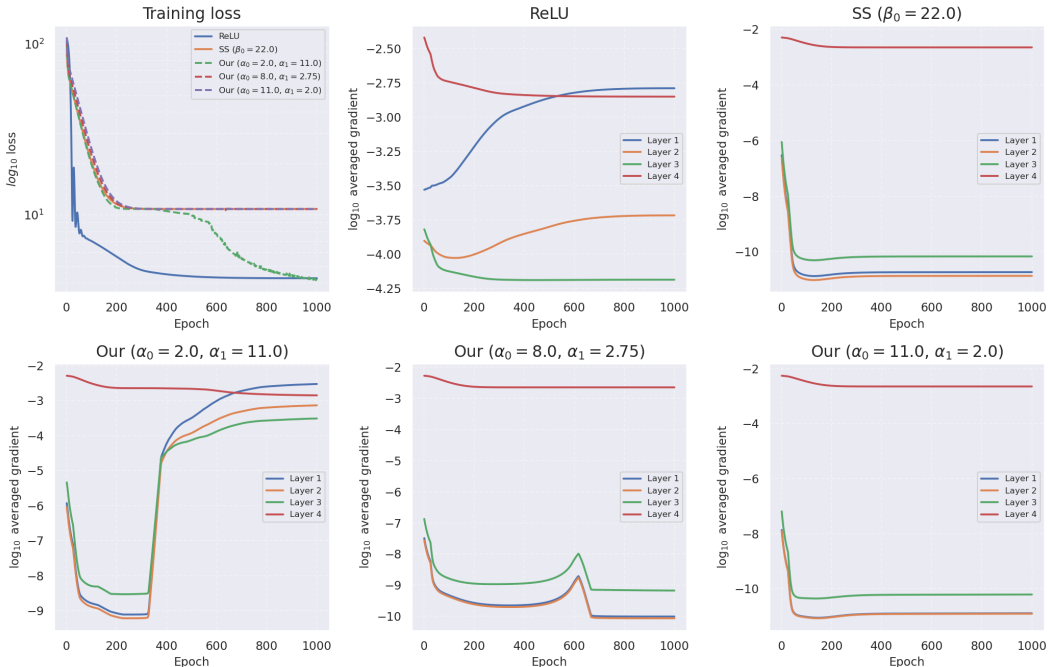


Figure 7: Plots of the loss and the logarithm of the average L2 norm of the gradients over epochs for all models.

F.2.2 Analysis of vanishing gradients in various DNN architectures

In this section, we conduct experiments to evaluate the vanishing gradient phenomenon in DNNs when using HTAF, ReLU, and Scaled Sigmoid as activation functions. We set $\alpha_0 = 3$, $\alpha_1 = 7.3$ and $\beta_0 = 22$. We consider various DNN architectures. Here, we do not apply batch normalization to each layer. Experiments are conducted on ABALONE dataset.

As described in Appendix F.2.1, we compute the average gradient with respect to the pre-activations at each layer across various DNN architectures. We investigate the occurrence of gradient vanishing using the average gradients from the first layer closest to the input. The results are reported in Figure 8 and Table 7. Here, we consider gradient vanishing to occur when the L2 norm of the average gradient value in the first layer is smaller than 10^{-5} . Gradient vanishing consistently occurs when using Scaled Sigmoid, whereas it is not observed with ReLU. For HTAF, gradient vanishing emerges in networks with five hidden layers.

To mitigate this issue, we decrease α_0 while keeping the product $\alpha_0\alpha_1$ constant for DNNs with five hidden layers where gradient vanishing is observed. However, this adjustment does not consistently improve prediction performance, nor does it fully resolve the vanishing gradient problem.

In some cases, as shown in Appendix F.2.1, reducing α_0 alleviates gradient vanishing and leads to improved performance. Overall, these results suggest that tuning α_0 can partially mitigate gradient vanishing, but does not provide a complete solution.

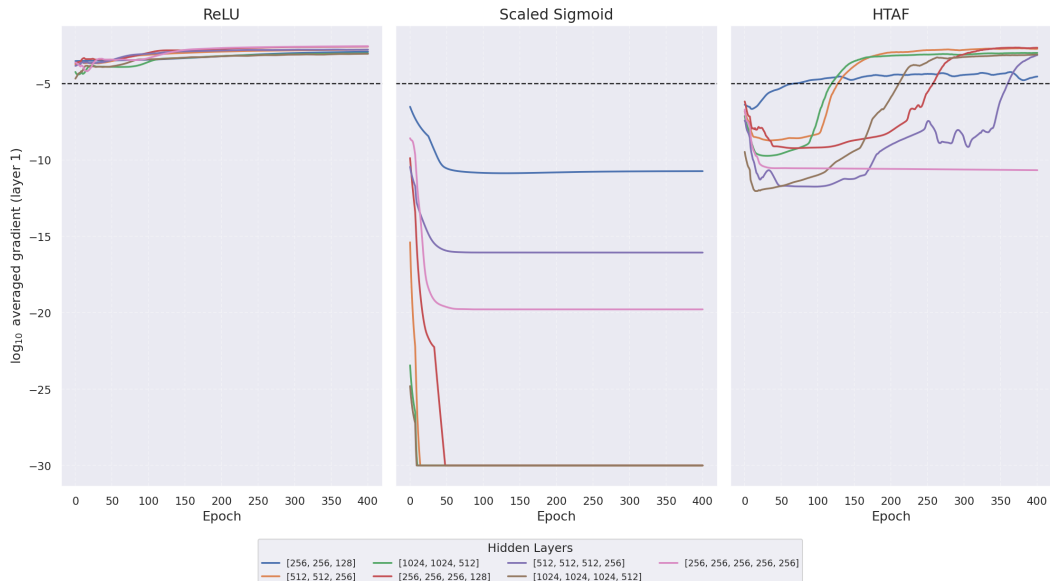


Figure 8: Plots of the logarithm of the average L2 norm of layer 1 gradients over epochs for all models.

Table 7: Results on the presence of gradient vanishing across different DNN architectures.

Hidden Layer Dimensions of the DNN	ReLU	HTAF	Scaled Sigmoid
[256, 256, 128]	X	X	O
[512, 512, 256]	X	X	O
[1024, 1024, 512]	X	X	O
[256, 256, 256, 128]	X	X	O
[512, 512, 512, 256]	X	X	O
[1024, 1024, 1024, 512]	X	X	O
[256, 256, 256, 256, 256]	X	O	O

F.3 Experiments on Deep Heaviside neural Networks for tabular datasets

In this section, we compare DHNs trained using our HTAF, STE and SS on tabular datasets including WINE, ABALONE, FICO and CHURN. The DNN architecture consists of three hidden layers with 256, 256, and 128 nodes.

During training, we replace all activation functions in the DNN with HTAF. For inference, we use the Heaviside function instead of HTAF. We refer this model as DNNs with HTAF. Similarly, we denote the DHN trained by approximating the Heaviside function with Scaled Sigmoid (SS) function as the DNN with SS. The DHN trained using STE method is referred to as the DHN with STE.

For α_0 , α_1 and β_0 , we choose optimal parameters from the candidate in Appendix D.4. For STE method, we use the candidate surrogate gradients in Appendix D.4.

For regression datasets, we use Root Mean Square Error (RMSE) and for classification datasets, we use Area Under ROC curve (AUROC) as the prediction performance measures. We divide the dataset into training, validation, and test sets with a 70/10/20 ratio. The validation set is used to determine the optimal hyperparameters, and the test set is used to evaluate the prediction performance of the trained models. We repeat this random splitting procedure five times to obtain five measures for prediction performance.

Table 8 presents that the averages and standard errors of the performance measurement of the DNN, the DNN with HTAF, the DNN with SS and the DHN with the STE on WINE, ABALONE, CHURN and FICO datasets. The results indicate that the DNN with HTAF achieves markedly better prediction performance than the DNN with SS and the DHN with STE method.

Table 8: Results of prediction performance on various tabular datasets.

Dataset	Measure	DNN	DNN + HTAF	DNN + SS	DHN + STE
WINE	RMSE ↓	0.693 (0.01)	0.730 (0.01)	0.745 (0.01)	0.794 (0.01)
ABALONE	RMSE ↓	2.003 (0.02)	2.106 (0.02)	2.403 (0.08)	2.620 (0.07)
CHURN	AUROC ↑	0.831 (0.01)	0.828 (0.01)	0.828 (0.02)	0.816 (0.01)
FICO	AUROC ↑	0.787 (0.01)	0.778 (0.01)	0.778 (0.01)	0.773 (0.01)

F.4 Experiments on Deep Heaviside neural Networks for Large Language Models

In this section, we evaluate the effectiveness of replacing activation functions in LLM with HTAF on commonsense reasoning tasks. We consider two approaches. First, we replace the activation function with HTAF during training and revert it to the Heaviside activation function at inference time. We refer this approach as HTAF method. Second, we replace the activation function with the Heaviside function and train the model using STE. We refer this approach as STE method.

We use the pre-trained Llama-2-7b ([67]) and Qwen-3.5-9b ([53]) models as the backbone architectures, initialized from the pretrained checkpoints provided at <https://huggingface.co/meta-llama/Llama-2-7b-hf> and <https://huggingface.co/Qwen/Qwen3.5-9B>, respectively. The decoders of both Llama-2-7b and Qwen-3.5-9b consist of 32 layers, each of which contains a feedforward module with the SwiGLU ([63]) activation function. To analyze the impact of HTAF in deep layers, we progressively replace the activation functions in the last k layers of the decoder, where k takes values in $\{4, 8, 12, 16, 20, 24, 28, 32\}$. We consider three common-sense reasoning benchmarks : Winogrande-small (WG-S, [59]), Winogrande-medium (WG-M, [59]), OpenBookQA (OBQA, [47]).

We apply both HTAF method and STE method to the pre-trained Llama-2-7b and the pre-trained Qwen-3.5-9b, and fine-tune the model on each dataset using Low-Rank Adaptation (LoRA, [24]). For training, we use the AdamW optimizer with a linear learning rate scheduler, a warmup ratio of 0.06, and a learning rate of 10^{-4} . For hyperparameters of LoRA, we use rank $r = 8$ and scaling factor $\alpha = 16$, and each stage is trained for 5,000 steps.

Figure 9 presents the accuracies of Llama-2-7b and Qwen-3.5-9b as a function of k . As k increases, the overall prediction performance of the model degrades; however, the HTAF method exhibits a smaller performance drop compared to the STE method. These results suggest that HTAF provides a more stable alternative when replacing activation functions with the Heaviside function in LLMs.

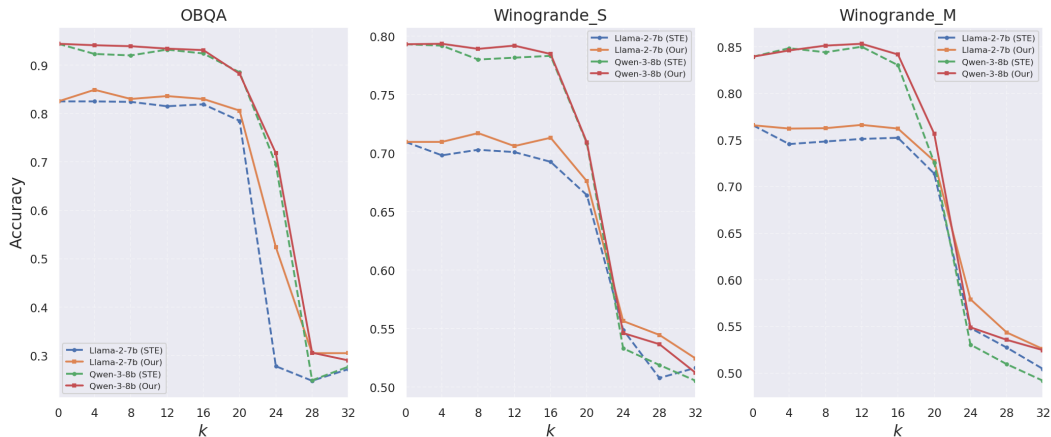


Figure 9: Results of the prediction accuracy of LLM depends on various k .

G Additional Experiments for ICBM

G.1 Additional results in Section 4.2.3

Here, we provide the LLM responses for each node described in Section 4.2.3.



Figure 10: Images of *Bewick Wren*.

135th node. *Bewick's Wren* is a terrestrial perching bird that typically forages in brush, shrubs, woodland edges, bark crevices, and dense vegetation, searching for small insects and other invertebrates. Hence, they are likely to be activated.

LLM Response

Distinguishing Concept

Ecomorphological Niche: Terrestrial Woodland Foragers vs. Aquatic, Marine, and Aerial Specialists

The primary concept that separates these two groups is their ecological niche, which dictates their habitat, morphological adaptations (bill shape, foot structure), and foraging strategies. Group A consists entirely of land-dwelling perching birds adapted to forests and brush, while Group B is heavily dominated by waterbirds, seabirds, and birds adapted to high-speed aerial hunting.

186th node. Since *Bewick's Wren* has slender, pointed, slightly decurved bill suited for precisely capturing small insects and invertebrates, it is likely to be activated in the node.

LLM Response

Distinguishing Concept

Bill Morphology: Hooked/Spear-like vs. Stout or Conical

The primary concept separating these two groups is the functional morphology of the bill. Group A is characterized by bills specialized for capturing mobile prey, including wide gapes for aerial insect capture, hooked bills for grasping or tearing prey, and spear-like bills for plunge-diving. In contrast, Group B is characterized by bills adapted for applying mechanical force, such as stout conical bills for cracking seeds and sturdy chisel-like bills for excavating wood.

690th node. *Bewick's Wren* belongs to unactivated group because it is a cryptic, substrate-bound thicket dweller: it lives in dense woody cover, probes bark and leaf litter for hidden insects.

LLM Response

Distinguishing Concept

Ecological Biome Dependency: Grassland/Prairie Avifauna vs. Thicket, Shrubland, and Wetland Avifauna

The defining concept here is the macro-habitat and vegetative density these birds require to survive and breed. Group A represents an ecological guild deeply tied to open, low-growth environments (prairies, agricultural fields, and tundra). Group B represents a guild dependent on dense, woody secondary growth (briars, thickets, and scrub) or aquatic/riparian zones.

153rd node. The *Bewick's Wren* firmly belongs to the unactivated group because its preference for dense, brushy habitats aligns with that group's thicket-dwelling ecological profile.

LLM Response

Distinguishing Concept

Bill Ecomorphology & Foraging Mechanics: Precision Snatching & Gleaning vs. Mechanical Extraction & Crushing

The defining concept that separates these two groups is the structural engineering of their bills and the physical force they apply to secure food. Group A is characterized by "light-duty," highly precise bills designed to snatch exposed, unarmored food (like flying insects or swimming fish) using speed and agility. Group B is characterized by "heavy-duty" or highly specialized bills designed to apply significant mechanical force to break into armored food sources (wood, hard seeds, pine cones) or probe deeply into tight crevices.

217th node. As can be seen in Figure 10, *Bewick's Wren* lacks the bright yellow carotenoids that define the unactivated group, it is more likely to be activated in the node.

LLM Response

Distinguishing Concept

Visual Plumage Pigmentation: Yellow/Carotenoid Dominance vs. Structural, Melanin, and Red Coloration

While there are ecological differences between the two groups, the most defining and unifying factor-particularly in datasets categorizing these specific bird species (such as the CUB-200 ornithology dataset)-is their visual appearance, specifically the dominant color of their plumage. Group B is overwhelmingly characterized by bright yellow plumage (driven by dietary carotenoids), whereas Group A is defined by the absence of yellow, featuring structural blues, deep reds, and heavily melanistic grays, blacks, and browns.

Bewick Wren exhibits neither 'has_primary_color::black' nor 'has_wing_color::orange', and is therefore activated at this node.

G.2 Definition of importance score for the estimated implicit concept

Let $\mathbf{c} = (c_1, \dots, c_N) \in \{0, 1\}^N$ be an implicit concept vector (i.e., the outputs of the feature extractor), where N is the number of nodes in the final layer of the feature extractor. Since the classifier is a linear model, for a given class k , the logit value is defined as

$$\text{logit}(k) = \sum_{j=1}^N w_{j,k} c_j + b_k, \quad (17)$$

where $w_{j,k}$'s are the weights and b_k is the bias of the linear model.

That is, the importance of each estimated implicit concept is quantified via Linear model’s weights. Specifically, we define the importance score of the estimated implicit concept of the j th node for class k as the absolute value of weight, i.e., $|w_{j,k}|$. Higher importance score indicates that the corresponding node contributes more significantly to the classification of the given class.

G.3 Additional results for class-specific activation values

In this section, we provide additional results for all classes corresponding to the experiment in Section 4.2.2 on CIFAR-10 dataset. Figure 11 presents these results. It implies that the implicit concepts estimated by ICBM are highly class-specific, whereas those learned by a standard image model are not.

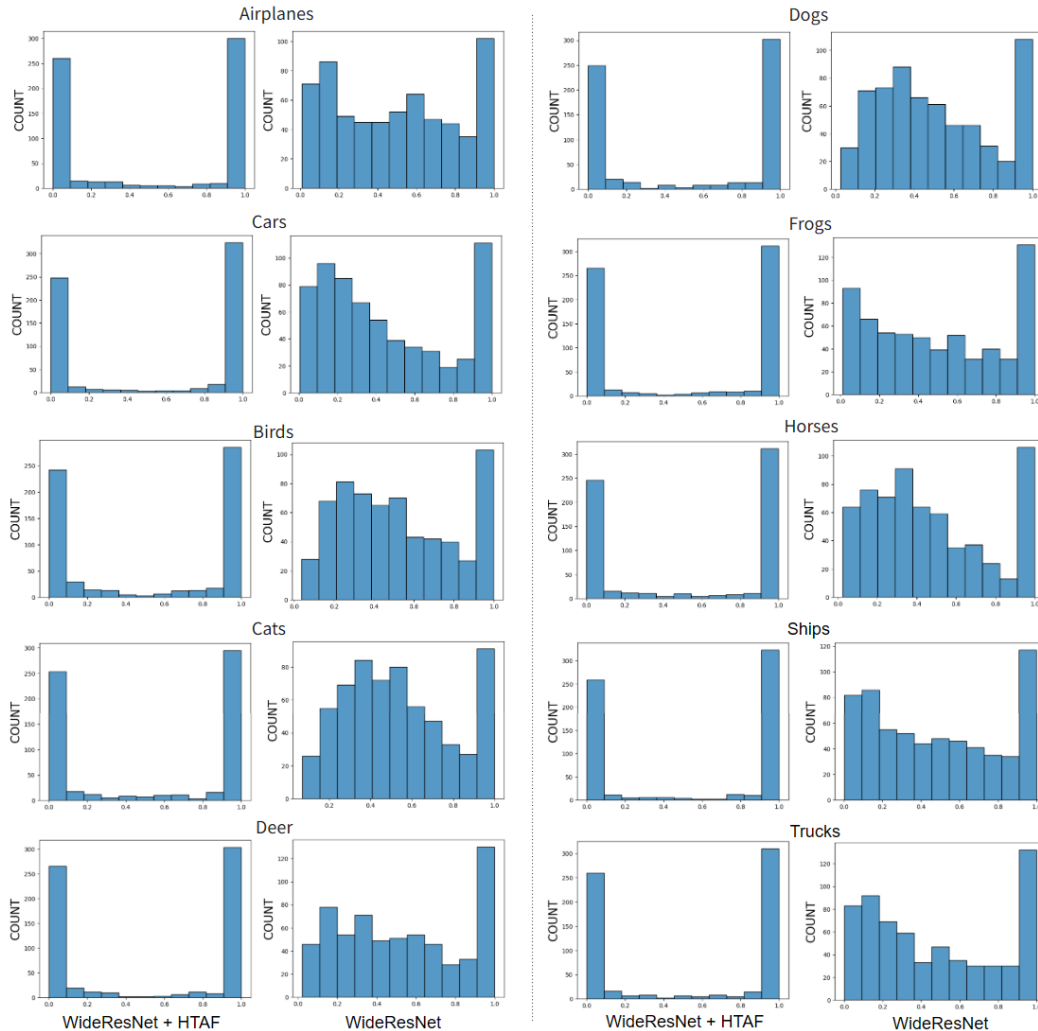


Figure 11: Histograms of the proportions for all classes.

G.4 Additional experiments on Heaviside approximation and concept meaningfulness

In this section, we evaluate whether our method approximates the Heaviside activation function while achieving strong prediction performance. We also investigate whether the estimated implicit concepts contribute meaningfully to the classification decision.

To measure how close the activation outputs are to zero or one, we use binarity score, defined as *the proportion of activation outputs that are greater than 0.99 or less than 0.01*. Higher binarity score indicates that the activation is closer to the binary representations.

Table 9: Comparison between HTAF, SS, STE and BM.

Dataset	Measure	HTAF	SS				STE	BM
			$(\beta_0 = 10^1)$	$(\beta_0 = 50)$	$(\beta_0 = 10^2)$	$(\beta_0 = 10^3)$		
CIFAR-10	Accuracy	96.1%	95.5%	95.7%	95.3%	79.3%	94.3%	90.0%
	Binarity score	98.4%	3.9%	40.4%	73.3 %	99.7 %	100.0%	-
	Concept accuracy	96.1%	91.2 %	91.6%	91.5%	73.8 %	89.7%	88.4%
CIFAR-100	Accuracy	79.5%	77.8%	78.6%	78.2 %	56.3%	74.8%	70.7%
	Binarity score	98.3%	14.3 %	60.5%	74.0 %	99.8%	100.0%	-
	Concept accuracy	84.6%	77.0%	78.7%	78.8%	67.8%	76.1%	70.8%

Furthermore, we evaluate whether the implicit concepts estimated by ICBMs capture meaningful information for image classification under the following assumption: if the presence or absence of an estimated implicit concept can be predicted from the true class labels of images, then the concept is likely to encode semantically meaningful information for classification. Therefore, for each node, we train a logistic regression model to predict the absence of the estimated implicit concept using only the true class label as input. We measure the meaningfulness of the implicit concepts estimated by the model by averaging the accuracies across all nodes, and refer to this metric as a concept accuracy. A higher concept accuracy indicates that the model estimates more meaningful implicit concepts.

We use WideResNet as the backbone model and conduct experiments on the CIFAR-10 and CIFAR-100 datasets. We consider four methods, including ours, as follows:

- HTAF : The activation function in the final layer of the feature extractor is replaced with HTAF during training, and the outputs are binarized at inference time.
- SS : The activation function in the final layer of the feature extractor is replaced with Scaled Sigmoid during training, and the outputs are binarized at inference time.
- BM : At inference time, the outputs of the feature extractor are binarized based on a median threshold.
- STE : Replaces the activation with the Heaviside function and trains it using Straight-Through Estimator (STE).

For all methods, hyperparameters are chosen as described in Appendix D. For BM, the training-related hyperparameters are tuned in the same manner as in the other methods. Table 9 presents the averages of accuracies, binarity scores and concept accuracies for all methods.

We observe that HTAF achieves the best overall performance across all metrics. For SS, binarity score increases as β_0 becomes larger; however, training becomes unstable, leading to degraded prediction performance. In the case of BN, replacing the activation function with the Heaviside activation function at inference time substantially degrades prediction performance.

G.5 Effect of post-binarization on model prediction performance

We conduct an additional experiment to assess the impact of inference-time binarization, defined as replacing the activation function with the exact Heaviside function during inference. Specifically, we measure how much the prediction performance degrades after this replacement. We set the WideResNet as the backbone image model and consider CIFAR-10 and CIFAR-100 datasets. Table 10 presents the average accuracy before and after inference-time binarization for HTAF, SS, and BM defined in Appendix G.4, over five trials. We observe that HTAF exhibits the smallest degradation in prediction performance after binarization, indicating that it is more robust to replacing the activation function with the exact Heaviside function at inference time.

Table 10: Averaged accuracy before and after inference-time binarization.

Dataset	HTAF		SS		BM	
	Before	After	Before	After	Before	After
CIFAR-10	96.1%	96.1%	96.1%	95.7%	95.6%	90.0%
CIFAR-100	79.5%	79.5%	79.0%	78.7%	79.2%	70.7%

G.6 Analysis of representations by HTAF

In this section, we analyze the outputs of the feature extractor in ICBMs when using HTAF compared to ReLU. We use the CIFAR-100 dataset, and adopt WideResNet as the backbone image model. Figure 12 presents the histogram of feature extractor outputs aggregated over all feature dimensions and all samples in the test dataset. We observe that, when using HTAF, most of the feature extractor outputs are concentrated near zero or one, whereas this behavior is not observed when using ReLU.

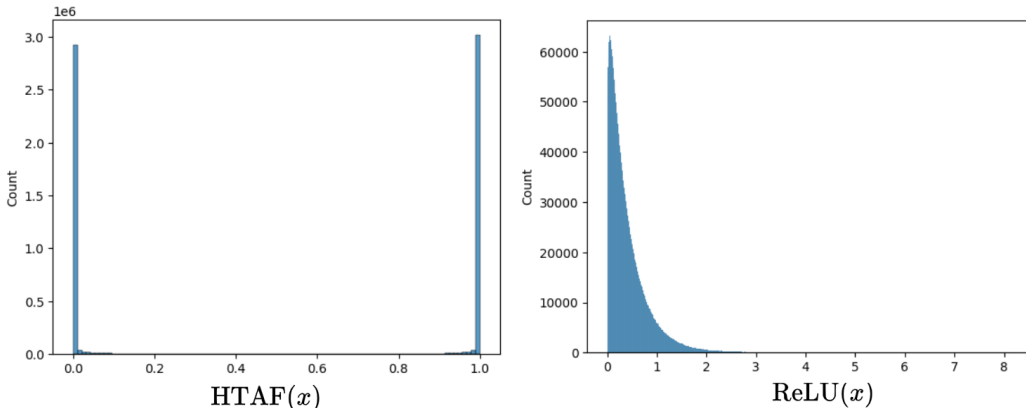


Figure 12: Plots of the outputs for HTAF and ReLU.

G.7 Comparison with CBMs

Here, we conduct additional experiment to compare ICBMs with original CBMs ([32]) and Label-free CBMs ([50]) on CIFAR-10, CIFAR-100 and CUB-200 datasets. The backbone image model is set to WideResNet. For Label-free CBMs, we use the official code provided by [50], with minor modifications. For CBMs, we implement the model from scratch. We employ SGD as the optimizer with a learning rate of 10^{-4} . All other hyperparameters for Label-free CBMs are set to the default values in the official code. Table 11 presents the prediction performance of ICBMs, CBMs, and Label-free CBMs. The best results are highlighted in **bold**. For CIFAR-10 and CIFAR-100 datasets, original CBMs cannot be trained due to the absence of concept annotations. As shown in the table, ICBMs achieve substantially higher prediction performance compared to baseline methods.

Table 11: Results of accuracies of CBMs, Label-free CBMs and ICBMs on CIFAR-10, CIFAR-100 and CUB-200 datasets.

Model	CIFAR-10	CIFAR-100	CUB-200
CBMs	–	–	72.5%
Label-free CBMs	86.5%	65.1%	55.7%
ICBMs (Ours)	96.1%	79.5%	77.3%